RESEARCH ARTICLE

Key Points:
- Seismic imaging of thermohaline structure in upper 1,000 m of Gulf of Mexico
- Diapycnal diffusivity from tracked reflections using fine-scale parametrization
- Mixing enhanced above shoaling bathymetry of continental slope

Correspondence to:
A. Dickinson,
nad38@cam.ac.uk

Spatial Variation of Diapycnal Diffusivity Estimated From Seismic Imaging of Internal Wave Field, Gulf of Mexico

Alex Dickinson[1] [ID], N. J. White[1] [ID], and C. P. Caulfield[2,3] [ID]

[1]Bullard Laboratories, Department of Earth Sciences, University of Cambridge, Cambridge, UK, [2]BP Institute, University of Cambridge, Cambridge, UK, [3]Department of Applied Mathematics and Theoretical Physics, University of Cambridge, Cambridge, UK

Abstract Bright reflections are observed within the upper 1,000 m of the water column along a seismic reflection profile that traverses the northern margin of the Gulf of Mexico. Independent hydrographic calibration demonstrates that these reflections are primarily caused by temperature changes associated with different water masses that are entrained into the Gulf along the Loop Current. The internal wave field is analyzed by automatically tracking 1,171 reflections, each of which is greater than 2 km in length. Power spectra of the horizontal gradient of isopycnal displacement, ϕ_{ξ_x}, are calculated from these tracked reflections. At low horizontal wave numbers ($k_x < 10^{-2}$ cpm), $\phi_{\xi_x} \propto k_x^{-0.2 \pm 0.6}$, in agreement with hydrographic observations of the internal wave field. The turbulent spectral subrange is rarely observed. Diapycnal diffusivity, K, is estimated from the observed internal wave spectral subrange of each tracked reflection using a fine-scale parametrization of turbulent mixing. Calculated values of K vary between 10^{-8} and 10^{-4} m^2 s^{-1} with a mean value of $K \sim 4 \times 10^{-6}$ m^2 s^{-1}. The spatial distribution of turbulent mixing shows that $K \sim 10^{-7}$ m^2 s^{-1} away from the shelf edge in the upper 300 m where stratification is strong. Mixing is enhanced by up to 4 orders of magnitude adjacent to the shoaling bathymetry of the continental slope. This overall pattern matches that determined by analyzing nearby suites of CTD casts. However, the range of values recovered by spectral analysis of the seismic image is greater as a consequence of significantly better horizontal resolution.

1. Introduction

Mechanical mixing within the oceans is a significant component of global thermohaline circulation (Wunsch & Ferrari, 2004). It is generally recognized that internal waves transfer energy from the large-scale flow to small length scales, at which turbulence irreversibly dissipates kinetic energy (Ferrari & Wunsch, 2009). This turbulence drives small-scale overturning, which mixes properties across density gradients. Mixing is commonly parametrized in terms of the diapycnal diffusivity, K (Montgomery, 1939). Using an advective-diffusive balance, Munk (1966) argues that the globally averaged value of K is 10^{-4} m^2 s^{-1}.

Over the past fifty years, K has been estimated in different ways. On basin-wide scales, K is inferred by tracking the spread of inert tracers injected into the water column (e.g., Ledwell et al., 1998). On fine scales (i.e., $\sim O(1)$ m), K can be calculated using measurements of temperature and salinity as a function of depth obtained from CTD casts, from towed and moored arrays, and from semiautonomous gliders (e.g., Klymak & Moum, 2007; Mauritzen et al., 2002). Finally, direct measurements of microscale (i.e., $\sim O(1)$ mm) fluctuations of temperature and particle velocity can be used to estimate K (e.g., Osborn & Cox, 1972; Polzin et al., 1997; Toole et al., 1994). Together, these observations suggest that, within the oceanic interior, K has an average and consistent value of 10^{-5} m^2 s^{-1} which contrasts with Munk's canonical value of 10^{-4} m^2 s^{-1} (Waterhouse et al., 2014). It is inferred that greater amounts of mixing are concentrated within regions of rough bathymetry at mid-ocean ridges and along continental shelves (e.g., Ledwell et al., 2000; Polzin et al., 1997).

Seismic (i.e., acoustic) imaging provides an important new tool with which to investigate the spatial and temporal variation of diapycnal mixing. Changes of temperature and salinity within the water column produce variations of acoustic impedance, which is the product of sound speed and density, that are detectable using standard seismic reflection profiling (Holbrook et al., 2003). Calibration with coincident

hydrographic measurements shows that seismic imaging is potentially sensitive to temperature contrasts as small as 0.03°C (Nandi et al., 2004). A significant advantage of this technique is that vertical and horizontal resolutions are both on the order of 5–10 m.

Over the past decade, seismic imaging has been used to examine a variety of oceanographic phenomena such as fronts, eddies, internal waves, and thermohaline staircases (e.g., Fer et al., 2010; Nakamura et al., 2006; Pinheiro et al., 2010). Furthermore, power spectral analysis of tracked seismic reflections has demonstrated that seismic imaging is capable of identifying internal wave and turbulent regimes (e.g., Holbrook & Fer, 2005; Krahmann et al., 2008). This capability can be used to measure diapycnal diffusivity (e.g., Falder et al., 2016; Fortin et al., 2016; Sheen et al., 2009).

Although a considerable amount of research has been carried out on the large-scale flow of water masses within the Gulf of Mexico, relatively little effort has focused on small-scale mixing processes. Ledwell et al. (2016) carried out a tracer-release experiment at a depth of $\sim$1,100 m in order to investigate spreading and dissipation of hydrocarbon fluid following an accidental spillage. They estimate a diapycnal diffusivity of order 10^{-4} m^2 s^{-1} across the continental slope of the northern Gulf of Mexico. They also found lower diffusivities ($K \sim 0.15 \times 10^{-4}$ m^2 s^{-1}) within the abyssal Gulf. Jing et al. (2015) analyze subthermocline diapycnal mixing in the northern Gulf using a fine-scale parametrization of observations acquired by moored Acoustic Doppler Current Profilers (ADCPs). In the wake of Hurricane Katrina, estimated diapycnal diffusivities of $K \sim 11.7 \times 10^{-5}$ m^2 s^{-1} are significantly elevated above the mean value of $K \sim 1.8 \times 10^{-5}$ m^2 s^{-1} obtained for hurricane-free periods. Wang et al. (2016) estimate turbulent kinetic energy dissipation rates and diapycnal diffusivities from microstructure profiles acquired in the vicinity of the Deepwater Horizon site in the northern Gulf (Figure 1a). They report enhanced dissipation rates of order 10^{-9} m^2 s^{-3} between 150 and 350 m and also between 1,100 and 1,300 m. However, small diffusivities of $K \lesssim 10^{-5}$ m^2 s^{-1} are obtained within the upper 500 m, probably as a consequence of strong stratification of the thermocline. Elevated diffusivities ($K \gtrsim 10^{-5}$ m^2 s^{-1}) are observed below $\sim$1,000 m, where the stratification is weaker.

Here we present and analyze a two-dimensional vertical seismic transect across the northern margin of the Gulf of Mexico. Our aims are threefold. First, we describe the reflective structure along this transect and relate it to the thermohaline structure and oceanographic setting of the Gulf of Mexico. Second, we show how spectral analysis of automatically tracked reflections can be used to identify the internal wave subrange with confidence. Third, we use these spectra to investigate the spatial pattern of diapycnal diffusivity.

2. Signal Processing

The seismic profile was acquired by ION Geophysical on 24 and 25 July 2002. This profile is a 175 km-long vertical slice through the water column that crosses the Sigsbee Escarpment (Figure 1a). It starts and ends in water depths of about 3,000 and 200 m, respectively. During seismic acquisition, the acoustic source consisted of a tuned airgun array with a volume of 4,800 in.^{3} which was primed with an air pressure of 2,000 psi. Reflected acoustic waves were recorded by a 9 km streamer towed at a depth of 9 m that had 360 hydrophones spaced every 25 m. The record sampling interval was 4 ms. The vessel steamed in a straight line with a speed of about 2.5 m s^{-1} and shots were fired every 50 m, yielding a fold of cover (i.e., redundancy) of 90. Sea-surface conditions were calm throughout the acquisition program.

The processing methodology used here exploits standard techniques that are adapted from those used to construct seismic images of the solid Earth (Yilmaz, 2001). There are three key processing steps. First, frequency filtering is used to reduce the influence of ambient noise. Randomly generated ambient noise is suppressed using a zero-phase, high-pass (i.e., >2 Hz) Butterworth filter. After this filtering, reflections from subsurface structure are muted. The direct wave and noise from other seismic sources in the area are removed using an adaptive filter. Seismic amplitudes are corrected for spherical divergence of the wave field as it propagates through the water column.

Second, individual shot records are sorted into common midpoint (cmp) records that are added together to generate a coherent seismic image with the best signal-to-noise ratio (a process called stacking). Seismic data are recorded as a function of the time that elapses between generation and detection of acoustic energy (i.e., two-way travel time). Before stacking, each cmp must be corrected for the progressive time delay which occurs between shots and receivers that are increasingly offset from each other. This normal
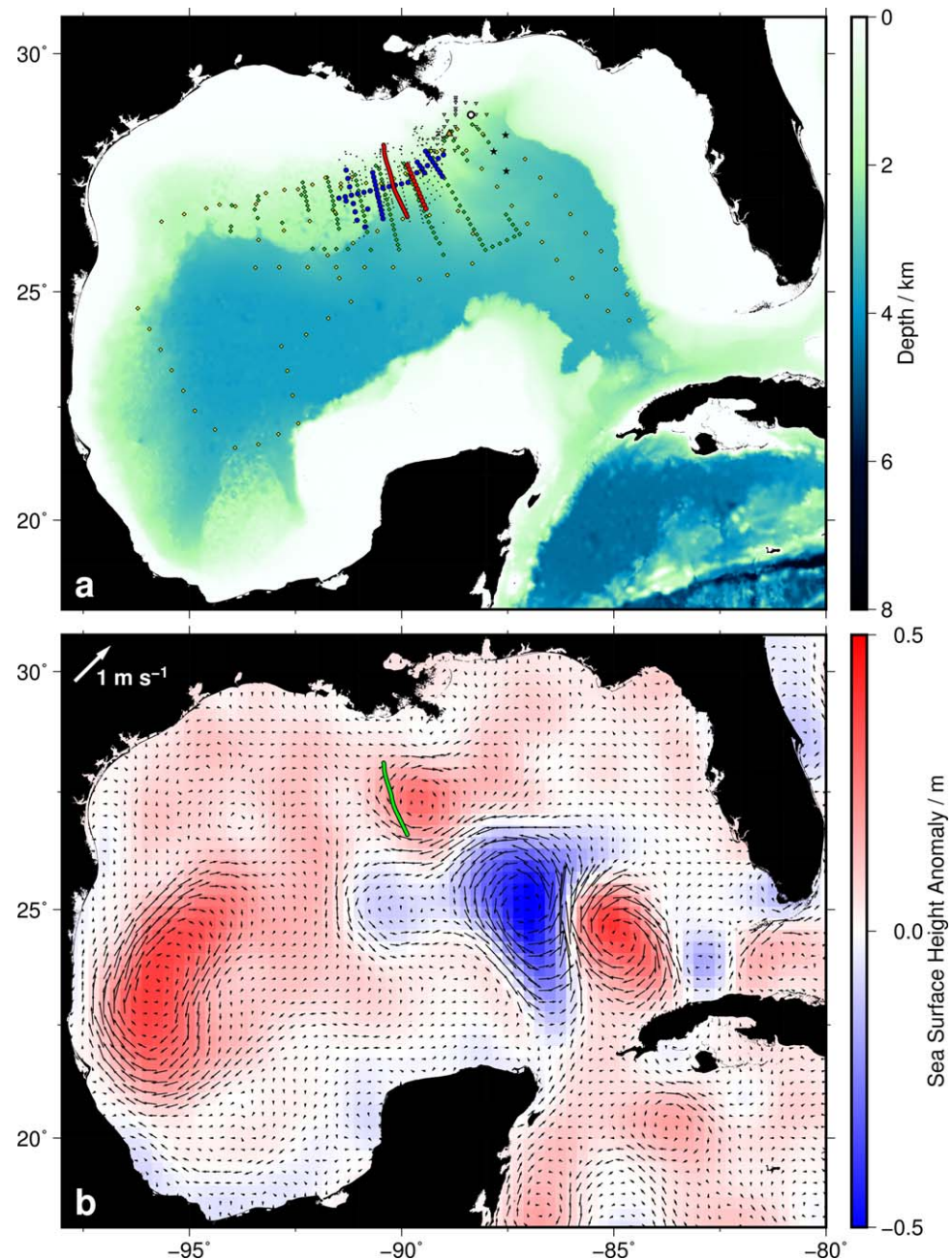
Figure 1. (a) Bathymetric map of Gulf of Mexico. Red line = seismic profile acquired between 24 and 25 July 2002; black dots = 249 regional CTD casts acquired in June–August of 1990–2010; blue circles = 63 CTD casts acquired by R/V *Pisces* between 22 August and 1 September 2010 (certain CTDs are repeated); red circles = subset of 12 CTD casts from transect acquired between 30 and 31 August 2010; black stars = loci of 3 ADCPs from 2005 experiment of Jing et al. (2015); gray inverted triangles = 22 microstructural profiles acquired during 2013 experiment of Wang et al. (2016); orange triangle = approximate location of tracer injection from 2013 experiment of Ledwell et al. (2016); green diamonds = loci of 4 month tracer measurements of Ledwell et al. (2016); yellow diamonds = loci of 12 month tracer measurements of Ledwell et al. (2016); white circle = location of accidental spillage at Deepwater Horizon platform. (b) Synoptic map showing 7 day average of sea-surface height anomalies straddling 24 July 2002. Black arrows = barotropic geostrophic velocity field (scale at top left-hand corner); green line = seismic profile crossing prominent anticyclonic eddy.

moveout correction relies on carefully choosing the root-mean-square (rms) sound speed of seawater as a function of two-way travel time for shot-receiver pairs that share a common point of reflection at depth. Although sound speed generally varies only between 1,470 and 1,530 m s^{-1}, these rms functions must be

chosen and applied with considerable care. Functions are selected directly from the seismic data by manually identifying values that maximise the coherency between seismic reflections observed at the same two-way travel time within a given cmp (a process called velocity picking). It is important that velocity picking is sufficiently dense (e.g., every 625 m in this case) to allow for horizontal changes in sound speed (Fortin & Holbrook, 2009). Excessive frequency stretching at distant offsets is minimized by applying a stretch mute of 1.5 (Yilmaz, 2001).

Finally, reflected signals must be repositioned within the spatial domain such that any diffracted energy is collapsed and dipping structures are accurately oriented. This process is known as migration and can be carried out either before or after the stacked image is constructed. It requires knowledge of sound speed as a function of two-way travel time. Sheen et al. (2009) carried out an iterative prestack depth migration. However, this form of prestack processing can degrade horizontal wave number spectra at higher wave numbers (Falder et al., 2016). Here we have carefully followed the recommendations of Holbrook et al. (2013) by carrying out poststack time migration with a standard frequency-wave number algorithm (Stolt, 1978). For display purposes, two-way travel times are then converted to depth using a constant sound speed of 1,500 m s^{-1} and the seismic image is horizontally smoothed using a 100 m-wide boxcar filter.

Temporal blurring inherent in acquisition of seismic reflection data can complicate interpretation (Klaeschen et al., 2009; Vsemirnova et al., 2009). Here 90 individual traces (i.e., time records) are assigned to each single cmp and are acquired during a time interval that lasts ~30 minutes. Application of the stretch mute excises traces that take the longest duration to record so that in practise deeper reflections within an individual cmp are imaged over an interval of ~7 minutes. Shallower reflections are imaged over even shorter intervals. A <7 minute interval is much shorter than the buoyancy period ($N{\lesssim}3$ cph below 250 m; Figure 7). As a result, we are confident that individual loci along a given reflection can be regarded as being close to stationary.

The final stacked image is characterized by numerous bright reflections that tilt southward (Figure 2a). These reflections are generated by thermohaline structure within the top 750–1,000 m. Progressively fainter reflections are visible down to a depth of ~1,200 m. Below ~1,200 m, reflections are barely visible. At depths of greater than 200 m, sinusoidal oscillations characteristic of an internal wave field are ubiquitous, especially above the continental slope (Figures 3a and 3e). A prominent lenticular structure with an aspect ratio of 100 ± 20 is visible at a range of 55 km and at a depth of 400 m (Figure 3c). Its aspect ratio is approximately the same order of magnitude as an estimated value of $N/f \sim 60$, suggesting that this structure is close to geostrophic balance and can be interpreted as an eddy.

3. Hydrographic Calibration

The observed reflectivity can be calibrated with the aid of regional CTD casts. All CTD profiles from the northern Gulf reveal a similar structure (Figure 4). The composition of the water mass within the upper ~1,000 m is determined by the Loop Current, a warm, saline mass of water that enters the Gulf through the Yucatan Channel. This current flows northwestward around Cuba before it exits through the Straits of Florida to form the Gulf Stream (e.g., Nowlin et al., 2001; Sturges et al., 2005). The near-surface mixed layer within the upper ~25 m is fresh as a result of a combination of dilution within the Caribbean Sea and of local influx of fresh water from the Mississippi River. Beneath this surficial layer, temperature decreases from ~30°C to ~5°C below ~1,000 m. Salinity decreases rapidly between ~100 and ~600 m, dropping to an approximately constant value of ~35.0 psu below ~1,200 m. A salinity maximum of ~36.7 psu occurs at a depth of 50–200 m and a salinity minimum of ~34.9 psu occurs at a depth of 600–900 m. These loci characterize warmer Subtropical Underwater and colder Antarctic Intermediate Water, respectively (Rivas et al., 2005). At intermediate salinities and temperatures, two additional water masses known as Sargasso Sea Water and Tropical Atlantic Central Water are identifiable. At depths greater than ~1,000 m, North Atlantic Deep Water, which has an almost constant temperature and salinity, fills the Gulf.

Within the upper ~600 m, sharp temperature contrasts of up to 1°C and salinity contrasts of up to 0.2 psu on vertical length scales of order 10 m are common, particularly within the upper ~200 m. Such contrasts are expected to give rise to clearly visible seismic reflections. Following the method described by Sallarès et al. (2009), estimations of the relative contributions of temperature and salinity to reflectivity based on CTD casts suggest that temperature is responsible for about 90% of the observed reflectivity structure
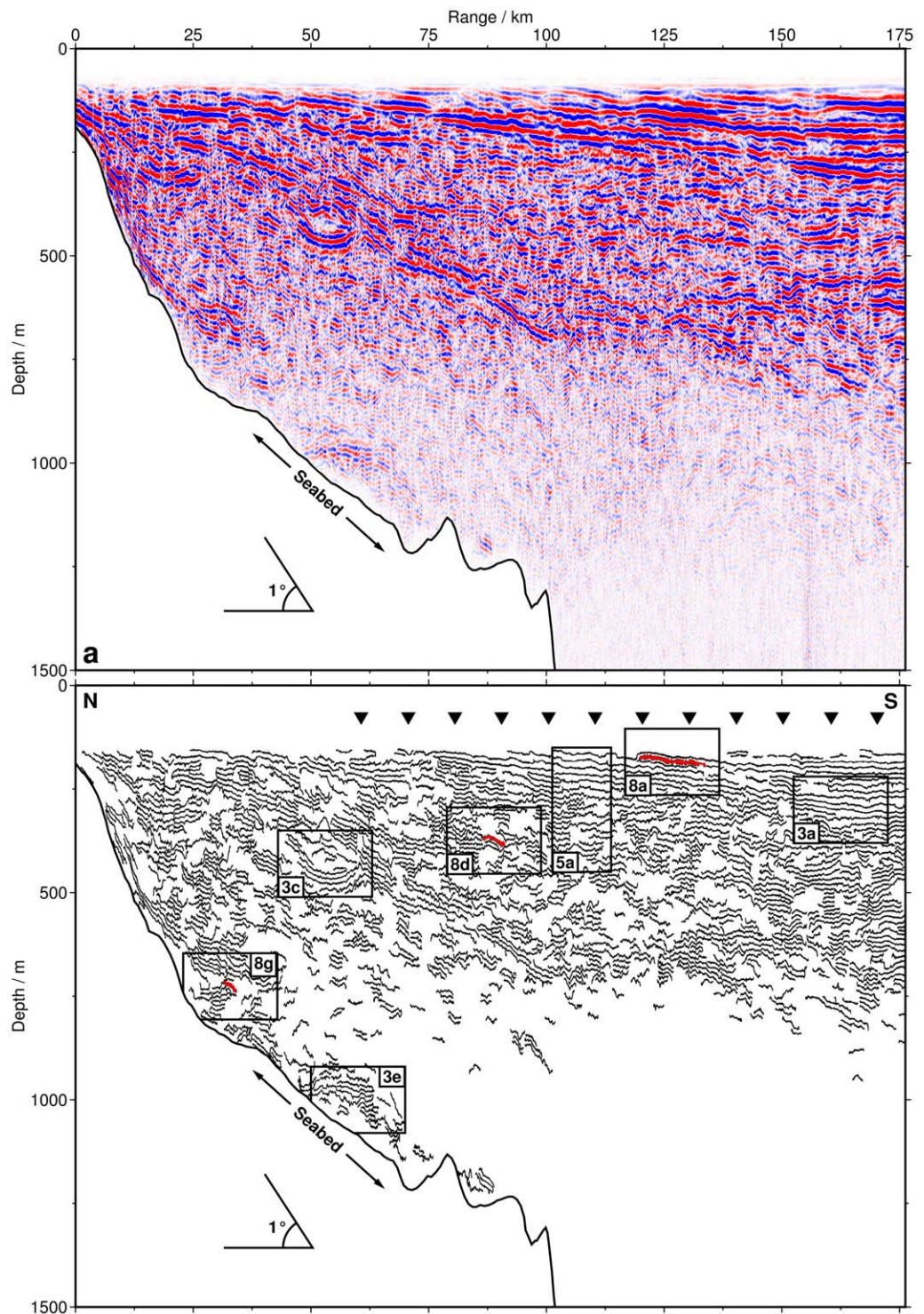
Figure 2. (a) Processed and stacked seismic profile plotted as function of range and depth. Red/blue events = reflective boundaries with positive/negative acoustic impedance; open triangle = 1° angle for reference. (b) 1,171 tracked reflections that are greater than 2 km in length (see text for details). Boxes labeled 3a, 3c, and 3e = loci of zooms shown in Figure 3; box labeled 5a = locus of zoom shown in Figure 5; boxes labeled 8a, 8d, and 8g with highlighted red reflections = loci of observed events that are spectrally analyzed in Figure 8; inverted black triangles = projected locations of 12 CTD casts acquired by R/V *Pisces* between 30 and 31 August 2010 (see Figure 1a).
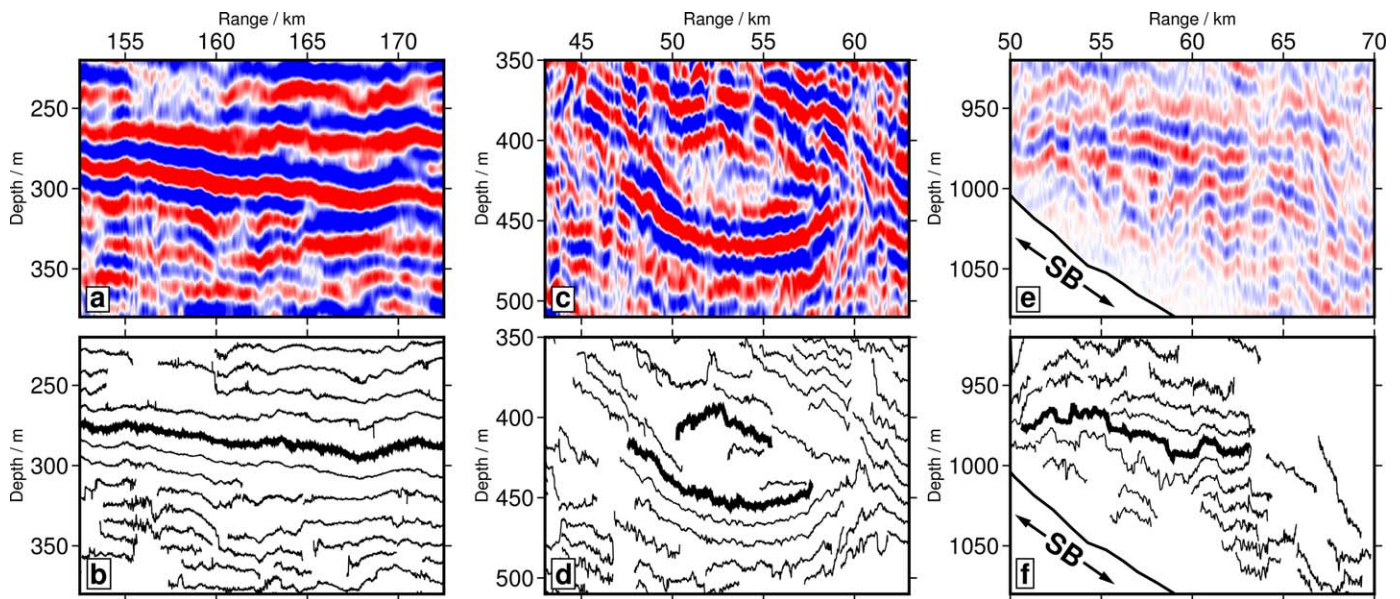
Figure 3. (a) Plot labeled 3a in Figure 2b. (b) Tracked reflections. Thick track = representative reflection showing internal waves with small amplitudes. (c) Plot labeled 3c in Figure 2b. (d) Tracked reflections. Pair of thick tracks = top and bottom of eddy showing differences in amplitudes of internal waves. (e) Plot labeled 3e in Figure 2b. SB = sea bed. (f) Tracked reflections. Thick track = representative reflection showing internal waves with large amplitudes.

between ∼100 m and ∼900 m. Below this depth, sharp temperature and salinity contrasts on seismically resolvable length scales are not observed.

Thus, the seismic image coheres with the pattern of reflectivity anticipated by analysis of hydrographic measurements. Submesoscale structures are imaged in detail at resolutions of order 10 m. In the upper ∼300 m, and especially to the south, reflections are strongly vertically layered and horizontally continuous
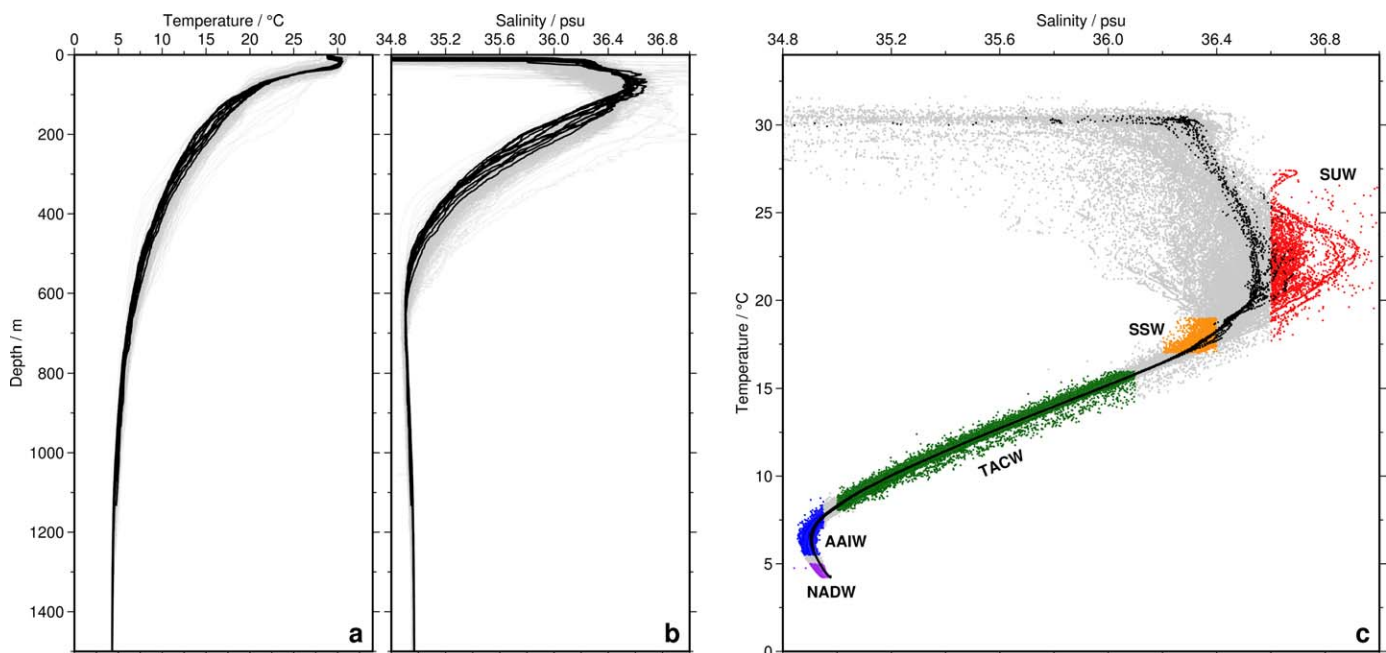

Figure 4. Temperature and salinity measurements from 324 CTD casts (see Figure 1a). (a) Temperature as function of depth. Black lines = 12 CTD casts along transect acquired by R/V *Pisces* between 30 and 31 August 2010; gray lines = other CTD casts. (b) Salinity as function of depth. (c) Temperature-salinity plot. SUW (red) = Subtropical Underwater; SSW (yellow) = Sargasso Sea Water; TACW (green) = Tropical Atlantic Central Water; AAIW (blue) = Antarctic Intermediate Water; NADW (purple) = North Atlantic Deep Water.

over distances of up to 80 km (Figure 3a). Elsewhere, particularly at greater depths and closer to the continental slope, reflections are usually shorter and more disrupted (Figure 3e). Qualitatively, this observation is suggestive of enhanced mixing at greater depths and closer to the shoaling continental slope due to reduced stratification and the proximity of rugose bathymetry.

4. Spatial Pattern of Diapycnal Diffusivity

The internal wave and turbulent fields possess distinctive distributions of kinetic and potential energy. These distributions are observable using horizontal wave number, k_x, power spectra of properties such as velocity fluctuation, density and temperature. For example, spectra of isotropic turbulence display a classical Kolmogorov exponent of $-5/3$ (Batchelor, 1959; Corrsin, 1951; Kolmogorov, 1941; Obukhov, 1949). In stratified fluids, isotropic turbulence is not expected to occur at length scales that are greater than the Ozmidov scale, L_O. This scale is an estimate of the largest vertical length scale that is unaffected by stratification (Ozmidov, 1965).

Recent analysis suggests that a regime of layered anisotropic stratified turbulence (LAST) exists at horizontal length scales greater than L_O and that this regime also exhibits a power spectral dependence of $k_x^{-5/3}$ (Riley & Lindborg, 2008). There is growing observational evidence that spectra consistent with the LAST regime occur in both atmospheric and oceanic data sets (e.g., Ewart, 1976; Falder et al., 2016; Klymak & Moum, 2007; Nastrom & Gage, 1985). At smaller wave numbers, displacements are dominated by the internal wave field. This field displays a dependence on wave number that is adequately described by the semiempirical Garrett-Munk spectrum, the first version of which appears in Garrett and Munk (1972, henceforth GM72). Internal wave spectra are red with exponents that vary between -2.5 and -2 for $10^{-3} \lesssim k_x \lesssim 10^{-2}$ cpm. To highlight the transition between internal wave and turbulent spectral subranges, horizontal wave number spectra are often multiplied by $(2\pi k_x)^2$ to yield horizontal gradient spectra (e.g., Klymak & Moum, 2007). On these transformed spectra, the internal wave regime remains red and the turbulent regime has an exponent of $+1/3$.

Spectral analyses of seismic profiles demonstrate that they are capable of imaging both internal wave and turbulent regimes (e.g., Holbrook & Fer, 2005). This capability has been exploited to estimate spatial patterns of diapycnal diffusivity (Falder et al., 2016; Fortin et al., 2016; Holbrook et al., 2013; Sheen et al., 2009). Here we extend and modify the methodology described by Falder et al. (2016) and use it to spectrally analyze vertical displacements of tracked seismic reflections. We note that accurate vertical spectra cannot easily be obtained from conventional seismic reflection images because acoustic impedance signals are convolved with the source wavelet which tends to be reverberatory. In future, this shortcoming could be addressed by carefully measuring the far-field source response, which would facilitate shot-by-shot deterministic deconvolution to successfully remove source-generated reverberations.

4.1. Preliminaries

Two initial steps must be carried out to ensure that a given seismic image is suitable for estimating robust values of diapycnal diffusivity. First, spectral content of the image is assessed using direct data transforms (Holbrook et al., 2013). At any given depth, the horizontal wave number spectrum of seismically observed amplitudes is calculated. Summation of spectra over a range of depths and multiplication by $(2\pi k_x)^2$ yields a horizontal gradient spectrum. Figure 5 shows a direct data transform spectrum for a panel taken from the seismic profile. White noise with an exponent of $+2$ dominates for k_x greater than 0.01 cpm, which demonstrates that in this case 75% of the observable wave number range is obscured (note that the Nyquist wave number is 0.04 cpm). The dominance of white noise at these wave numbers is evident throughout the seismic image and does not vary with frequency content. Consequently, the turbulent subrange is mostly obscured but negative slopes at lower values of k_x suggest that the image contains useful information about the internal wave field. Harmonic noise spikes are clearly visible at 0.02 and 0.04 cpm (Holbrook et al., 2013). Since these noise spikes only affect wave numbers already dominated by white noise, we have chosen not to remove them.

Second, we analyze the frequency content of the seismic image by defining the signal-to-noise ratio between two adjacent traces as
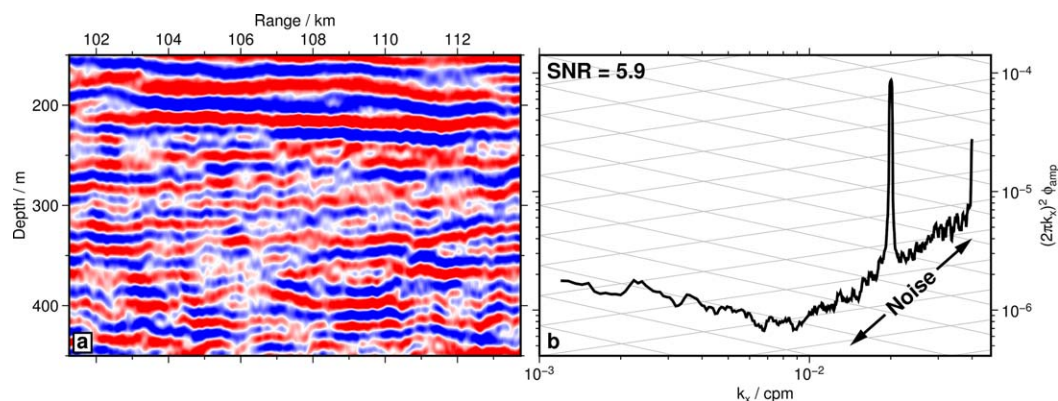
Figure 5. (a) Seismic image plotted as function of range and depth showing box labeled 5a from Figure 2b. Seismic panel has signal-to-noise ratio of 5.9. (b) Direct data transform of image shown in 5a plotted as function of horizontal wave number, k_x Gray reticule = slopes of representative internal wave field (gradient of −0.5) and of turbulence (gradient of +1/3); negative slope for $k_x < 10^{-2}$ cpm represents internal wave field; positive slope for $k_x > 10^{-2}$ cpm represents white noise (gradient of +2); spikes at $k_x = 2 \times 10^{-2}$ and 4×10^{-2} cpm represent harmonic noise. Note that slope of observed white noise is slightly smaller than expected due to minor loss of power at high wave numbers caused by frequency-wave number migration procedure.

$$SNR = \sqrt{\frac{|c|}{|a-c|}}, \qquad (1)$$

where c is the maximum value of the cross correlation between these traces, and a is the value of the zero-lag autocorrelation of the first trace (Holbrook et al., 2013). The signal-to-noise ratio for a given panel is gauged using the median value of signal-to-noise ratios for adjacent traces. Thermohaline structure is generally visible for frequencies lower than ∼60 Hz and the signal-to-noise ratio is greater than 4 for frequencies of 20–40 Hz. These observations suggest that the stacked seismic image should be filtered using a trapezoidal filter with corner frequencies of 10–20–40–50 Hz. Different filters do not significantly alter the results presented here (Appendix A). After band-pass filtering, the seismic image has a vertical resolution of approximately 10 m.

4.2. Spectral Analysis of Tracked Reflections

The reflections shown in Figure 2a can now be spectrally analyzed. The brightest reflections are tracked by contouring a constant value of the cosine of the instantaneous phase angle, a seismic attribute that emphasizes reflective continuity (Barnes, 2007; Holbrook et al., 2013). Here reflections greater than 2 km in length are exploited, ensuring that each wave number spectrum contains at least 20 points below a noise threshold of 0.01 cpm. Contouring of the 0.6 value of the cosine of the instantaneous phase angle yields the most reliable tracking database. We do not track reflections in the upper 150 m due to poor spatial resolution. A total of 1,171 reflections with a cumulative track length of 5,070 km are analyzed (Figure 2b). Our results are not significantly affected if reflections longer than 4 km are subdivided into shorter lengths of 2–4 km (Appendix A).

At present, it is not straightforward to determine the extent to which these seismic reflections track isopycnal surfaces. Previous studies suggest that seismic reflections probably do track isopycnal surfaces over distances of at least 8 km (Biescas et al., 2014; Holbrook et al., 2013; Krahmann et al., 2009; Sheen et al., 2011). We note that the analysis presented here does not depend on an exact coincidence between reflections, which strongly correlate with temperature gradients, and isopycnal surfaces. It is reasonable to assume that both isothermal and isopycnal surfaces are perturbed in a similar way by the internal wave field.

The power of vertical displacement, ϕ_ξ, as a function of k_x is calculated from each linearly detrended tracked reflection using a multitaper Fourier transform (Thomson, 1982). For the specified multitaper parameters and minimum track length, spectral leakage is only significant over, at most, 0.002 cpm. Variances of the estimated values of $\log_{10}(\phi_\xi)$ are determined following the approach described by Percival and Walden (1993). These variances are of the order of 0.15 logarithmic units (Appendix A). Holbrook et al. (2013) recommend using a constant sound speed to convert seismic images from two-way travel time to depth prior to

estimation of power spectra. Here we first calculate power spectra in terms of two-way travel time. Values of power at the lowest four wave numbers are removed in order to reduce spectral roll-off. Spectral amplitudes are then expressed in terms of depth displacement using an average depth-dependent sound speed profile that is computed using CTD casts. An uncertainty of ± 30 m s^{-1} for sound speed yields an error of ± 0.02 logarithmic units in $\log_{10}(\phi_\xi)$. Finally, multiplication of ϕ_ξ by $(2\pi k_x)^2$ enables the power of the horizontal gradient of vertical displacement, ϕ_{ξ_x}, to be plotted as a function of k_x.

On each power spectrum, we have carefully identified internal wave, turbulent and white noise spectral subranges by fitting an appropriate model to the spectrum in $\log_{10}(k_x)$-$\log_{10}(\phi_{\xi_x})$ space. Due to the onset of noise at relatively low wave numbers, few spectra with turbulent subranges were identified with confidence. Spectral values below a noise threshold of $k_x < 10^{-2}$ cpm probably correspond to displacements caused by the internal wave field.

It is important that these low-wave-number subranges are directly compared with previous observations and with the Garrett-Munk internal wave spectrum. Measurements by towed instruments suggest that, for $10^{-3} \lesssim k_x \lesssim 10^{-2}$ cpm, horizontal wave number spectra are reasonably approximated by a power law that takes the form

$$\phi_{\xi_x} \propto k_x^p, \qquad (2)$$

where p is within the range of -0.5 to 0 (e.g., Bell, 1976; Katz, 1973; Katz & Briscoe, 1979; McKean & Ewart, 1974; Müller et al., 1978; Zenk & Katz, 1975). Based on such observations, a revised version of the GM72 model proposed by Garrett and Munk (1975, henceforth GM75) exploits a power law description where $p = -0.5$ at the limit of high horizontal wave number (i.e., $k_x \gtrsim 10^{-2}$ cpm).

Subsequent modifications of the GM model are based mainly on observations of shear and strain obtained from vertical profiles that include white strain spectra at the limit of high vertical wave number (Cairns & Williams, 1976, henceforth GM76; Gregg & Kunze, 1991, henceforth GK91). Nonetheless, integration of GM76 and GK91 over frequency and vertical wave number yields horizontal wave number spectra similar to those observed.

In order to compare our results with previous work, we follow the approach of Klymak and Moum (2007) and fit a straight line to each low-wave-number subrange in $\log_{10}(k_x)$-$\log_{10}(\phi_{\xi_x})$ space using least squares linear regression. A weighted histogram of the fitted gradients shows that the distribution of mainly negative exponents has a prominent peak with a weighted mean of $\bar{p} = -0.2 \pm 0.6$ (Figure 6). These predominantly negative spectral slopes suggest that the observed spectral subranges at low wave numbers (i.e., $k_x < 10^{-2}$ cpm) do indeed correspond to the internal wave field.
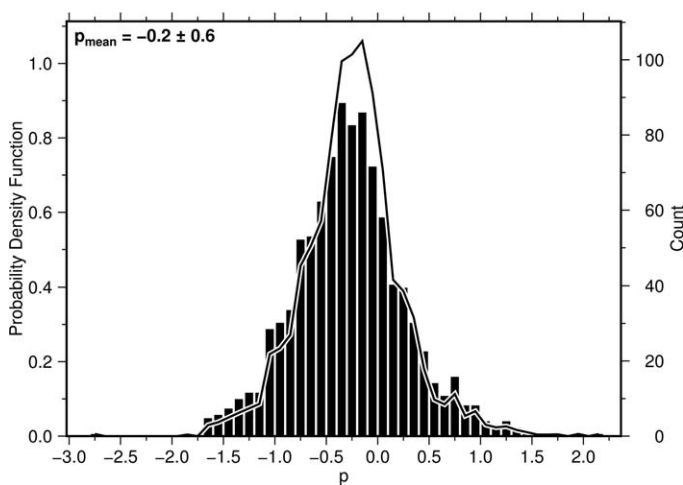
We can now estimate mixing rates from these internal wave spectral subranges. Several authors have attempted to relate energy of the internal wave field to the rate of dissipation of turbulent kinetic energy, ϵ (e.g., Gargett & Holloway, 1984; McComas & Müller, 1981; Munk, 1981). The most commonly used approaches exploit parametrizations based on the theoretical and numerical analysis of Henyey et al. (1986). This analysis predicts that ϵ depends quadratically both on the energy of the internal wave field and on N. ϵ also has a weak dependence on latitude (Gregg et al., 2003). The Henyey et al. (1986) model has been applied to empirical spectra of both shear and strain (e.g., Gregg, 1989; Wijesekera et al., 1993). It has also been modified to account for non-GM wave fields (Polzin et al., 1995, 2014). Estimates of ϵ are determined by reference to the dissipation rate, ϵ_r, of a GM spectrum at a specified buoyancy frequency, N_r, and at a given latitude with a Coriolis parameter f_r. Here we use

$$\epsilon = \epsilon_r \left(\frac{\bar{N}}{N_r}\right)^2 \frac{f \operatorname{arccosh}(\bar{N}/f)}{f_r \operatorname{arccosh}(N_r/f_r)} \frac{R_{\omega_{GM}}}{R_\omega} \frac{(R_\omega + 1)}{(R_{\omega_{GM}} + 1)} \sqrt{\frac{R_{\omega_{GM}} - 1}{R_\omega - 1}} \hat{E}^2, \qquad (3)$$

where $\bar{N}$ is the local mean stable stratification, f is the local Coriolis parameter, R_ω is the local shear-strain ratio, $R_{\omega_{GM}} = 3$ is the shear-strain

Figure 6. Histogram of gradient measurements, p, for straight lines fitted to low-wave-number ($k_x < 10^{-2}$ cpm) spectral subranges for 1,171 tracked reflections in $\log_{10}(k_x)$-$\log_{10}(\phi_{\xi_x})$ space. Black bars = binned values of gradient measurement count (right-hand axis) and of probability density function (left-hand axis); solid line = weighted probability density function where weighting coefficients depend on uncertainty in straight line fitting. Distribution has weighted mean of $\bar{p} = -0.2 \pm 0.6$ consistent with internal wave field regime.
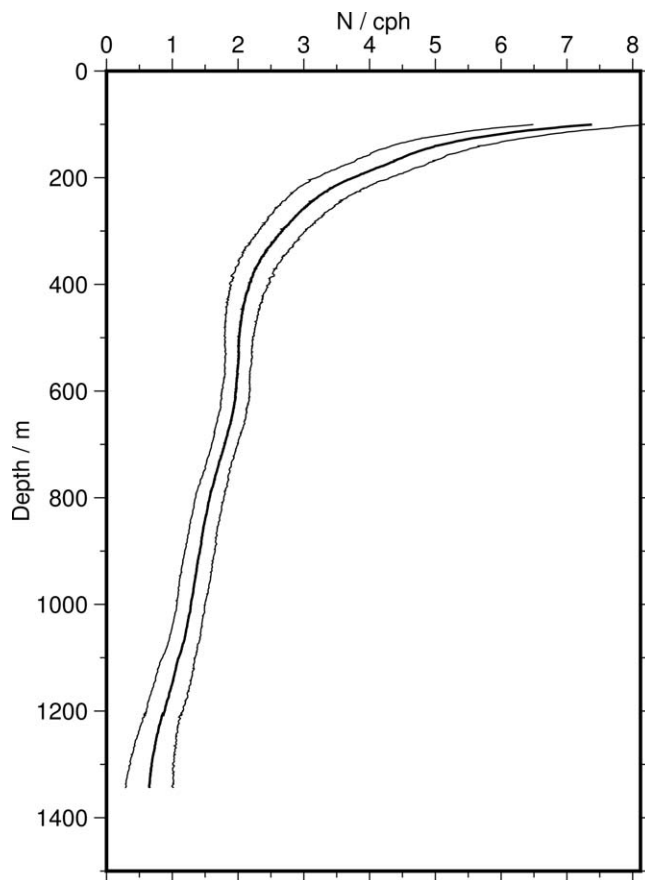
Figure 7. Buoyancy frequency, N, calculated from temperature and salinity measurements presmoothed using 100 m-long boxcar filter for 324 CTD casts (Figure 4). Thick/thin lines = average $N \pm 1\sigma$ as function of depth.

ratio of the GM wave field, and $\hat{E}$ is a measure of the energy of the observed wave field (Polzin et al., 2014). $\hat{E}$ is evaluated in terms of horizontal gradient spectra using

$$\hat{E} = \frac{R_\omega}{R_{\omega_{GM}}} \hat{\phi}_{\xi_x} = \frac{R_\omega}{R_{\omega_{GM}}} \frac{\langle \phi_{\xi_x} \rangle}{\langle \phi_{\xi_x}^{GM} \rangle}, \quad (4)$$

where $\phi_{\xi_x}^{GM}$ is the GM spectrum for the local value of the buoyancy frequency, $\bar{N}$. Angular brackets denote integration over the wave number range of the internal wave subrange ($k_x < 10^{-2}$ cpm). Due to the lack of local measurements of R_ω, we use the globally averaged value of R_ω $= 7 \pm 3$ of Kunze et al. (2006). f is assumed to be constant and is calculated using the latitude at the center of the seismic line, 27.4°N. $\bar{N}$ is taken to be the buoyancy at the average depth of each tracked reflection, which is obtained from an averaged regional profile (Figure 7).

Following Gregg et al. (2003), we compare observed dissipation rates with those predicted by a GM model at 30° latitude with $N_r = 3$ cph. We choose GM76 as the reference spectrum with a mode number scale $j_\star = 4$ and a high wave number saturated subrange in the vertical spectra for vertical wavenumbers $k_z > 0.1$ cpm. Equation (3) now becomes

$$\epsilon = 7.2 \times 10^{-10} \left(\frac{\bar{N}}{N_r} \right)^2 \frac{f \, \text{arccosh}(\bar{N}/f)}{f_r \, \text{arccosh}(N_r/f_r)} \frac{R_\omega(R_\omega+1)}{12} \sqrt{\frac{2}{R_\omega-1}} \frac{\langle \phi_{\xi_x} \rangle^2}{\langle \phi_{\xi_x}^{GM} \rangle^2} \quad (5)$$

with units of m² s⁻³.

The diapycnal diffusivity, K, is estimated from ϵ using the Osborn relationship

$$K = \frac{\frac{g}{\rho} \langle w'\rho' \rangle}{\frac{-g}{\rho} \frac{d\rho}{dz}} = \frac{B}{\bar{N}^2} = \frac{\Gamma \epsilon}{\bar{N}^2}, \quad (6)$$

where g is gravitational acceleration, ρ is mean density, ρ' is density perturbation, w' is vertical component of the velocity perturbation, B is buoyancy flux, and Γ is the dissipation flux coefficient (Osborn, 1980). Angular brackets denote averaging over time. This method assumes a balance between turbulent production, dissipation, and work done against buoyancy for the case of a statistically steady flow. Following convention, we assume a constant dissipation flux coefficient of $\Gamma = 0.2$, which represents the upper bound proposed by Osborn (1980). It is now recognized that the assumption of constant Γ is undoubtedly a significant simplification (e.g., Mashayek et al., 2017).

We have computed ϵ and K for each one of the 1,171 observed internal wave subranges. Example spectra and corresponding values of p and K are summarized in Figures 8 and A1. The spatial distribution of K across the seismic image is shown in Figure 9. Calculated diapycnal diffusivities vary by 4 orders of magnitude. In the south, $K \sim 10^{-8}$ to 10^{-6} m² s⁻¹ with notably low diffusivities in the upper ~300 m. Higher values (K up to ~10^{-4} m² s⁻¹) are observed within the central and northern parts of the image, particularly just above the seabed. This spatial distribution is plausible since diapycnal mixing is probably inhibited by strong stratification within the upper ~300 m and enhanced in the vicinity of rugose bathymetry. Nonetheless, it is important to analyze the effect that random and systematic uncertainties have on these results.

4.3. Error Analysis

To start with, we assume that the method for estimating ϵ from ϕ_{ξ_x} using an internal wave parametrization of turbulent mixing is appropriate. Therefore, the uncertainty in the value of K can be assigned using uncertainties in values of $\hat{\phi}_{\xi_x}$, in physical parameters (i.e., $\bar{N}$, f, R_ω, and Γ), and in the chosen reference spectrum, $\phi_{\xi_x}^{GM}$. Further details of our approach to error analysis are described in Appendix A.
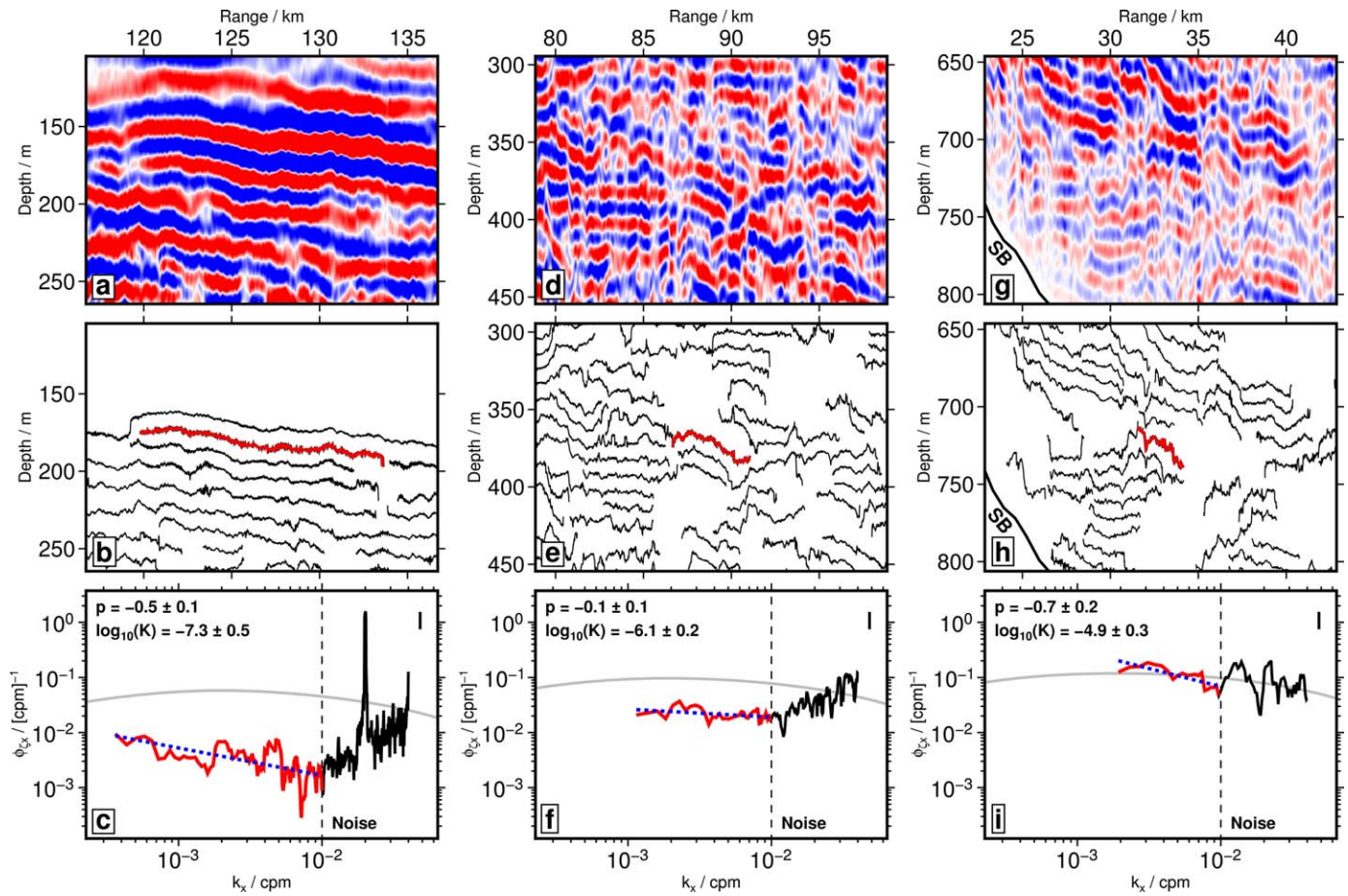
Figure 8. (a) Seismic panel corresponding to box labeled 8a in Figure 2b. (b) Same plot where reflections greater than 2 km in length have been tracked. Red line = tracked reflection used for spectral analysis. (c) Horizontal gradient spectrum of highlighted reflection in Figure 8b. Black/red line = observed spectrum with identified internal wave subrange; vertical dashed line = white noise cutoff at $k_x = 0.01$ cpm indicated by direct data transform (see Figure 5); solid gray line = GM76 reference spectrum; blue dashed line = straight line with gradient of p fitted to internal wave subrange; vertical bar at right-hand side = 95% confidence interval for ϕ_{ξ_x} (centered on $\phi_{\xi_x} = 10^0$ (cpm)$^{-1}$) calculated using method described by Percival and Walden (1993); optimal value of p and calculated value of $\log_{10}(K)$ shown in top left-hand corner (quoted uncertainty in K based solely on standard deviation of $\left(\phi_{\xi_x}/\phi_{\xi_x}^{GM}\right)$ for internal wave subrange). (d–f) Seismic panel, tracked reflections and spectrum for box labeled 8d in Figure 2b. (g–i) Seismic panel, tracked reflections and spectrum for box labeled 8g in Figure 2b. SB = seabed.

The uncertainty in $\hat{\phi}_{\xi_x}$ is estimated from the standard deviation of $\left(\phi_{\xi_x}/\phi_{\xi_x}^{GM}\right)$ for the wave number range of integration. Corresponding uncertainties in $\log_{10}(K)$ are between 0.13 and 1.6 logarithmic units (mean uncertainty is 0.5 ± 0.2 logarithmic units). We also test the accuracy of power spectral density estimations by varying the chosen multitaper Fourier transform parameters across a range of reasonable values. Estimates of $\log_{10}(K)$ for individual tracked reflections vary by up to 0.7 logarithmic units. It is important to emphasize, however, that the same spatial distribution of mixing is always recovered with K varying by a factor of $\sim 10^4$ across the seismic image.

Estimation of K from ϕ_{ξ_x} using equations (5) and (6) is only weakly dependent on local values of $\bar{N}$ and f. For a constant value of $f = 6.72 \times 10^{-5}$ rad s^{-1} and $\bar{N}$ between 1 and 4 cph, an uncertainty of ± 0.5 cph for $\bar{N}$ causes an uncertainty in $\log_{10}(K)$ of 0.5 logarithmic units or less. Likewise, our assumption of a constant value of $f = 6.72 \times 10^{-5}$ rad s^{-1} at a latitude of 27.4°N introduces a small uncertainty of ± 0.01 logarithmic units in $\log_{10}(K)$.

When determining the effects of uncertainties in R_ω and Γ, we have not formally propagated errors because the underlying distributions of R_ω and Γ are not known with sufficient accuracy. Instead, we explore the effects on K of choosing upper and lower bounds for R_ω and Γ. R_ω has a globally averaged value of 7 ± 3 for non-GM wave fields in the abyssal ocean (Kunze et al., 2006). Unfortunately, we have no means to estimate R_ω and we therefore assume a value of $R_\omega = 7$. The close correspondence between observed spectra
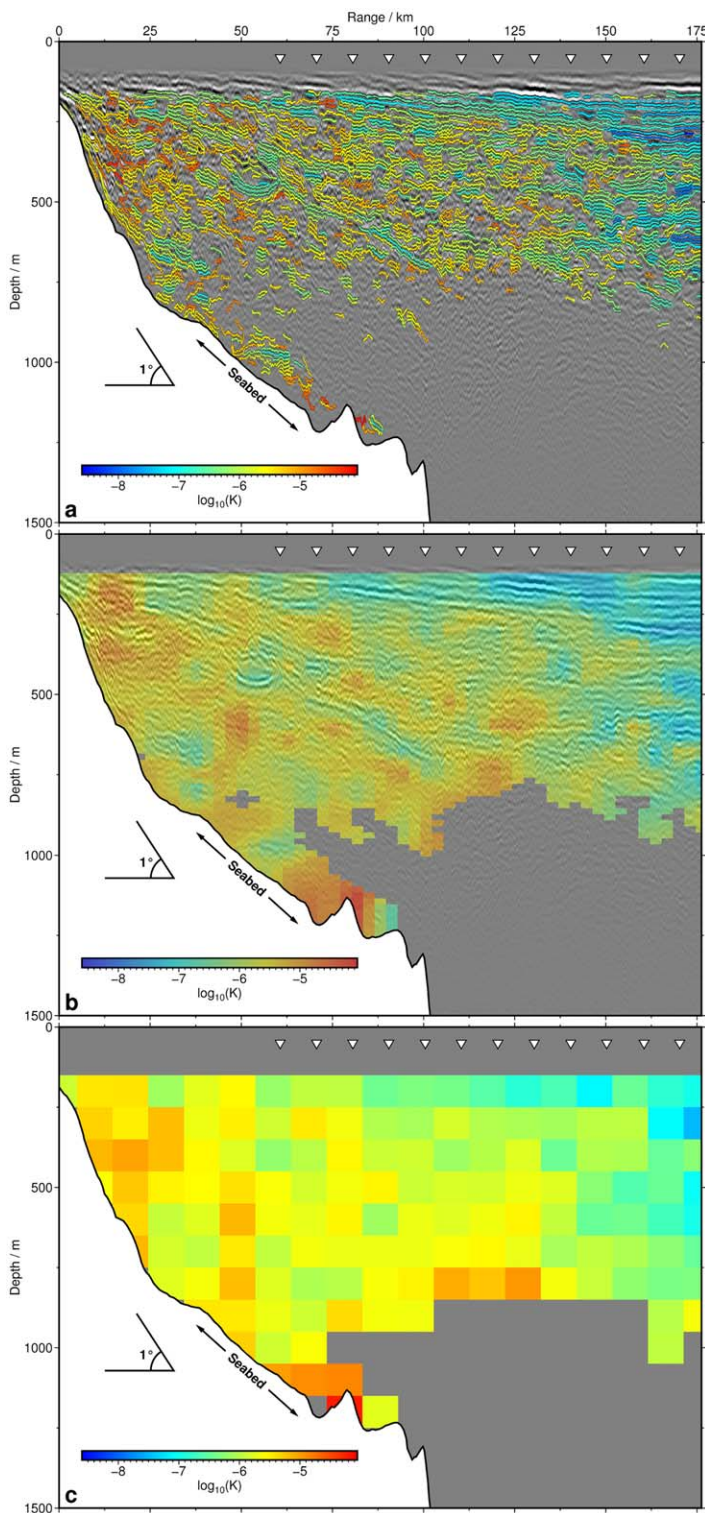
Figure 9. (a) Seismic image overlain with spatial pattern of diapycnal diffusivity calculated using internal wave spectral subranges of 1,171 tracked seismic reflections. Colored events = individually tracked reflections where color indicates value of $\log_{10}(K)$; inverted white triangles = projected locations of 12 CTD casts acquired by R/V *Pisces* between 30 and 31 August 2010 (see Figure 1a). (b) Seismic image overlain by interpolated and smoothed pattern of $\log_{10}(K)$. (c) Seismic image overlain by binned values of $\log_{10}(K)$ for comparison with Figure 10a.

and the GM76 model suggests that R_ω probably does not deviate significantly from the GM value of $R_\omega=3$ (Figure 6). Even if R_ω varies between 2 and 20, our assumption of $R_\omega=7$ introduces an uncertainty in $\log_{10}(K)$ of, at most, 0.6 logarithmic units. As a consequence, the calculated increase in K over the continental slope is probably real and not simply an artefact of a varying shear-strain ratio.

Γ cannot be regarded as constant and undoubtedly varies both temporally and spatially with higher values anticipated adjacent to oceanic boundaries (Mashayek et al., 2017). Taking lower and upper bounds of $\Gamma \sim 0.1$ and 0.4, respectively, implies that our assumption of a constant value of $\Gamma=0.2$ introduces an uncertainty in $\log_{10}(K)$ of up to 0.3 logarithmic units. We also note that, despite its pervasive usage, it is unclear whether or not the Osborn method represents a sufficiently accurate way to convert dissipation rates into diapycnal diffusivities within the oceanic realm, particularly if highly transient mixing events are under consideration (e.g., Ivey et al., 2008; Mashayek et al., 2013). Ignoring potential inaccuracies in the Osborn method, estimated uncertainties in $\bar{N}$, f, R_ω, and Γ are insufficient to account for the observed range of $\sim10^4$ in the magnitude of K across the seismic image.

Finally, estimations of K also depend on the choice of $\phi_{\xi_x}^{GM}$, the reference spectrum used for comparison with observed spectra. Many previous authors have used the GK91 model which is a minor modification of GM76. For comparison, we have computed diapycnal diffusivities using GK91 as $\phi_{\xi_x}^{GM}$. Individual values of $\log_{10}(K)$ vary by <0.11 logarithmic units compared to those computed using GM76 for $\phi_{\xi_x}^{GM}$.

We conclude by suggesting that it is reasonable to assign an approximate uncertainty of ±1 logarithmic units to recovered absolute values of $\log_{10}(K)$. Significantly, we propose that the observed spatial distribution of relative values of $\log_{10}(K)$ is robust to specific assumptions about power spectral density estimation, to uncertainties in the local physical variables, and to the choice of reference spectrum.

4.4. Independent Tests

We now consider the more fundamental question of whether ϵ can be reliably estimated from the horizontal gradient spectra of internal waves. First, we review the accuracy of fine-scale mixing parametrizations when applied to vertical wave number spectra. The model of Henyey et al. (1986) which underpins equation (3) has mostly been applied to vertical wave number spectra. Gregg (1989, henceforth G89) found that a fine-scale parametrization based on shear variance reproduces direct microstructural measurements of ϵ to within a factor of 2 at five midlatitude abyssal sites. Lee et al. (2006) report that values of ϵ estimated using the G89 parametrization agree to within a factor of 2 with those measured by microstructural profilers across the 3,000 m isobath of the Hawaiian Ridge.

Polzin et al. (1995, henceforth P95) modified the parametrization of Gregg (1989) to permit application to non-GM wave fields by including strain variance. They also included the latitudinal dependence predicted by Henyey et al. (1986). This dependence has been independently verified by Gregg et al. (2003) using a global suite of

microstructural measurements of ϵ. Naveira Garabato et al. (2004) compare fine-scale shear-strain estimates of ϵ computed from 141 CTD/ADCP profiles with results from three tracer-release experiments at different depths within the Greenland Sea. Estimates of K at these three depths agree to within a factor of 3.

Although fine-scale parametrizations were originally formulated for application to the deep ocean, they have also been successfully applied in other environments. For example, Nash et al. (2004) acquired profiles of fine-scale shear from instruments moored at three locations close to the 1,000 m isobath near the continental slope offshore the east coast of North America. Dissipation rates computed from these observations using the G89 scaling agree well with 245 profiles of ϵ acquired using nearby microstructural profilers. Fer et al. (2010) compute estimates of ϵ from observations of fine-scale shear and strain acquired within water depths of $\sim$1,000 m in the vicinity of the Yermak Plateau between Greenland and Svalbard. Dissipation rates estimated using the P95 parametrization agree with microstructural measurements within error.

In water depths of $\sim$150 m within the Storfjorden fjord of the Svalbard Archipelago, Fer (2006) finds that fine-scale shear-strain estimates of ϵ agree with microstructural measurements to within an average of 20%. However, MacKinnon and Gregg (2003) and Carter et al. (2005) find that the P95 parametrization fails in shallow water depths of <150 m above the New England and Monterey Bay shelves, respectively.

The P95 parameterization has also been applied to observations of strain that lack coincident measurements of shear by assuming that the shear-strain ratio is constant. Whalen et al. (2012) apply this fine-scale, strain-only, parametrization to a global database of temperature and salinity profiles acquired using Argo floats. These results are compared with microstructural measurements at six locations that include near the equator, above ridges, and near seamounts. Spatially averaged values of ϵ inferred from the fine-scale parametrization are found to agree within a factor of 3 with mean measured microstructural values in 96% of cases, provided that at least 10 data points contribute to each average fine-scale estimate. Frants et al. (2013) find that values of ϵ inferred from profiles of CTD strain in the Southern Ocean generally agree with microstructural measurements to within a factor of 4.

These different approaches suggest that fine-scale parametrizations of turbulent mixing are accurate to within at least an order of magnitude when averaged over a sufficiently large number of measurements of vertical spectra. In particular, the results of Nash et al. (2004) and of Fer et al. (2010) suggest that parametrizations perform well above continental slopes, the environment under consideration here. However, almost all previous tests of the parametrization have been made using vertical spectra of shear and strain. Klymak and Moum (2007) found a poor correlation between values of ϵ inferred from horizontal spectra of isothermal displacement and values of ϵ measured from microstructural shear probes. They reasonably concluded that application of a fine-scale strain parametrization to horizontal gradient spectra does not produce especially reliable estimates of ϵ.

We do not have coincident estimates of mixing against which to test our spectral results. However, in the summer of 2010 a comprehensive suite of CTD casts were acquired across the northern Gulf (https://data.nodc.noaa.gov/DeepwaterHorizon). A subset of these data was acquired by R/V *Pisces* between 22 August and 1 September 2010 and is of sufficiently high quality to be used for fine-scale strain parametrizations of turbulent mixing (Figure 1a). Here we estimate diapycnal diffusivities from these casts for comparison with seismically derived values.

Temperature and salinity were measured using the Seabird SBE 9 package. This instrument has quoted accuracies for temperature and conductivity of $\pm$0.001°C and $\pm$0.003 S m^{-1}, respectively. The sampling rate is 24 Hz, which yields a depth resolution of $\sim$0.04 m. We first removed erroneous values of temperature and salinity using the approach described in Appendix B. Corrected profiles were then sorted into 0.25 m-wide bins. Average values of temperature and salinity for each bin were computed. Data quality is assessed by constructing temperature and salinity spectra. Some spectra are noisy for wave numbers greater than $\sim$0.1 cpm. This noise does not affect the wave number range exploited when estimating turbulent mixing rates. Profiles of buoyancy frequency, N, are computed from these binned temperature and salinity profiles. Strain (i.e., the vertical gradient of vertical displacement, denoted by ξ_z) is given by

$$\xi_z = \frac{N^2 - N_s^2}{N_s^2},\qquad(7)$$

where N_s represents the stable, unperturbed buoyancy profile. Following the recommendations of Polzin

et al. (2014), N_s is estimated using adiabatic levelling calculated over a pressure range of 200 dbar (Bray & Fofonoff, 1981).

Strain profiles are divided into half-overlapping segments of length 200 m, and the strain spectrum, ϕ_{ξ_z}, is estimated for each segment. We exclude the upper 200 m in order to avoid contamination by rapidly varying near-surface salinity. ϵ and K are computed using equations (3) and (6), respectively. The energy level factor of equation (3) is given by

$$\hat{E} = \frac{R_\omega}{R_{\omega_{GM}}} \hat{\phi}_{\xi_z} = \frac{R_\omega}{R_{\omega_{GM}}} \frac{\langle \phi_{\xi_z} \rangle}{\langle \phi_{\xi_z}^{GM} \rangle},\tag{8}$$

where angular brackets denote integration over a specified wave number range and $\phi_{\xi_z}^{GM}$ is the reference GM strain spectrum. For consistency with seismically derived estimates, we choose GM76 as the reference spectrum with mode number scale $j_* = 4$ and a saturated subrange for $k_z > 0.1$ cpm. The limits of integration are chosen as 0.01 and 0.1 cpm, in order to avoid contamination by background stratification and by the high wave number saturated subrange, respectively (Frants et al., 2013). For each depth segment, we take the average value of N_s as $\bar{N}$ in equations (3) and (6). The local value of f is computed for each CTD cast.

Observed strain spectra compare well to the GM76 reference spectrum (e.g., Figures 10b–10d). For depth segments of length 200 m, 19 values of $\left(\phi_{\xi_z} / \phi_{\xi_z}^{GM} \right)$ lie within the wave number range of integration. The uncertainty in $\hat{\phi}_{\xi_z}$ is estimated from the standard deviation of these 19 values. Corresponding uncertainties in $\log_{10}(K)$ are between 0.09 and 2.2 logarithmic units (the mean uncertainty is 0.29 ± 0.13 logarithmic units). Different choices of multitaper transform parameters for a range of reasonable values have little discernable effect (individual values of $\log_{10}(K)$ vary by <0.5 logarithmic units). Diapycnal diffusivities are also computed using GK91 for $\phi_{\xi_z}^{GM}$. Values of $\log_{10}(K)$ vary by <0.07 logarithmic units and a similar spatial distribution of mixing is recovered. As before, the assumption of $R_\omega = 7$ introduces an uncertainty in absolute values of $\log_{10}(K)$ of 0.6 logarithmic units for R_ω varying between 2 and 20. The assumption of $\Gamma = 0.2$ introduces a further uncertainty of 0.3 logarithmic units.

A spatially coherent pattern of diapycnal diffusivity is recovered (Figure 10a). Low diffusivities ($10^{-6.5}$ m^2 s$^{-1} \lesssim K \lesssim 10^{-5}$ m^2 s^{-1}) extend as deep as $\sim$1,000 m in abyssal waters, south of the Sigsbee Escarpment. At greater depths, and above the rapidly shoaling seabed further north, diffusivities are elevated with values of K reaching 10^{-4} m^2 s^{-1}. The distribution of turbulent mixing computed from the CTD casts cannot be compared in detail with that recovered from the seismic image since the two data sets were acquired in different months and years (i.e., late July 2002 and late August 2010) and at different locations. Nevertheless, these different methodologies yield estimates that broadly agree at the largest scale. Both show generally low diffusivities within the highly stratified thermocline (upper $\sim$750 m). Both also show enhanced mixing associated with the rugose and shoaling bathymetry along the continental slope.

The two sets of results can be objectively and directly compared by constructing histograms of $\log_{10}(K)$ for the upper 800 m (Figure 11). This approach smooths out the observed spatial variation but enables the mean diapyncal diffusivity of the region to be examined. The two histograms show that distributions of $\log_{10}(K)$ computed from the seismic image and from CTD casts are both approximately normal with means of $[\log_{10}(K)]_{mean} = -5.9 \pm 0.7$ logarithmic units and $[\log_{10}(K)]_{mean} = -5.6 \pm 0.4$ logarithmic units, respectively. The two distributions of K are therefore approximately lognormal with mean diffusivities of $K \sim 4 \times 10^{-6}$ m^2 s^{-1}. The close agreement of these mean values suggests that both methods have accurately estimated the bulk diapycnal diffusivity of the thermocline.

Although the two distributions have similar means, the distribution of K estimated from the seismic image has both a greater range and a greater variance than that estimated from CTD casts. In particular, diapycnal diffusivities derived from the seismic image extend to much lower values ($K \gtrsim 10^{-8}$ m^2 s^{-1}) compared with those estimated from CTD casts ($K \gtrsim 10^{-6.5}$ m^2 s^{-1}). The increased range reflects in part the relative sizes of these two data sets (i.e., 1,078 tracked reflections within the upper 800 m versus 360 segments of CTD data within the upper 800 m). The greater variance may be a function of the enhanced sensitivity of the seismic methodology to localized changes in diapycnal diffusivity. Estimation of mixing rates from CTD casts necessarily involves division of buoyancy profiles into segments of finite vertical length (in this case 200 m). Within each of these segments, localized patches of turbulence tend to dominate the signal and regions of suppressed mixing may not necessarily be resolved. Moreover, discrete horizontal sampling of CTD data

($\sim O(10)$ km) is insufficient to fully characterize lateral submesoscale variations in diapycnal diffusivity. In contrast, vertical spatial resolution of the distribution of K estimated from the seismic image is limited by the vertical separation of discrete reflections ($\sim O(10)$ m). The horizontal spatial resolution is related to the
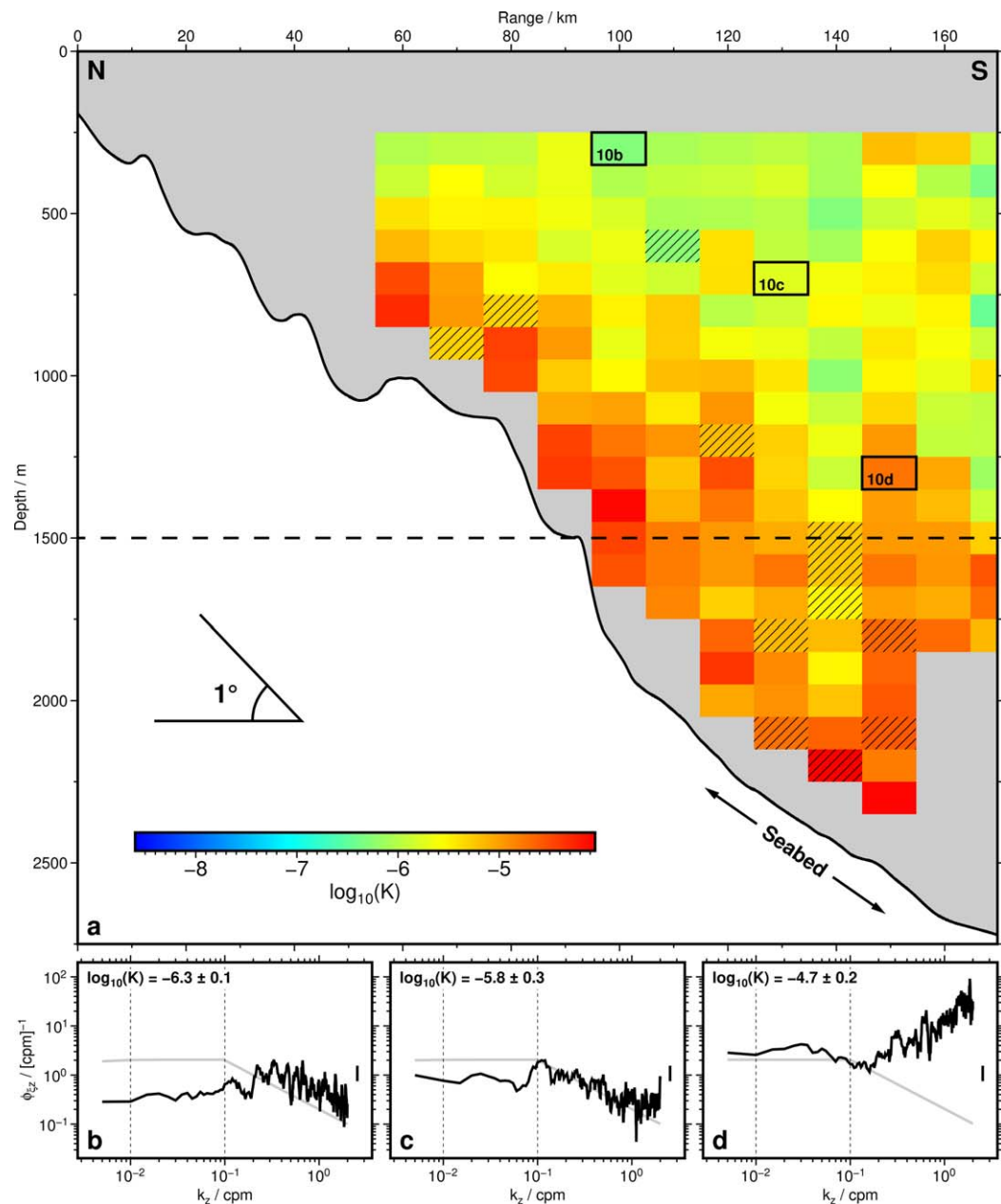

Figure 10. (a) Spatial pattern of diapycnal diffusivity calculated from 12 CTD casts acquired by R/V *Pisces* between 30 and 31 August 2010 (see Figure 1a). Colored boxes = values of $\log_{10}(K)$ calculated using method described by Polzin et al. (2014); dashed horizontal line at 1,500 m indicates depth range of seismic image (compare with Figure 9); boxes labeled 10b, 10c, and 10d = locations of spectra shown below; hashed boxes = less reliable estimates where uncertainty in log10(K) is greater than 0.5 logarithmic units based on standard deviation of $\left(\phi_{\xi_z} / \phi_{\xi_z}^{GM} \right)$ for wave number range of integration. (b) Vertical strain spectrum for box 10b. Black line = observed strain spectrum; gray line = GM76 reference spectrum; vertical dashed lines delimit wave number ranges of integration; vertical black line at right-hand side = 95% confidence interval for ϕ_{ξ_x} (centered on $\phi_{\xi_x} = 10^0$ (cpm)$^{-1}$) calculated using method described by Percival and Walden (1993); optimal value of $\log_{10}(K)$ shown in top left-hand corner (quoted uncertainty for $\log_{10}(K)$ based on standard deviation of $\left(\phi_{\xi_z} / \phi_{\xi_z}^{GM} \right)$ for wave number range of integration). (c) Vertical strain spectrum for box 10c. (d) Vertical strain spectrum for box 10d.

minimum length of tracked reflection necessary to construct well-resolved spectra (in this case 2 km). Over a certain depth range the horizontal resolution will be greater than that implied by a track length of 2 km since tracked reflections horizontally overlap. Therefore, the seismic image has the ability to capture changes in diapycnal diffusivity at horizontal and vertical resolutions that are superior to more sparsely located CTD casts. In particular, localized regions of low K, which may be obscured in the CTD estimate, are well resolved by the seismic image.

5. Discussion

Taken as a whole, our results suggest that turbulent mixing in the upper $\sim$800 m of the northern Gulf of Mexico is generally suppressed by high stratification of the thermocline (mean $K < 10^{-5}$ m^2 s^{-1}). Above the continental slope and at greater depths, mixing is enhanced by rugose bathymetry and by lower values of stratification, respectively ($K \lesssim 10^{-4}$ m^2 s^{-1}). The changes in seismic reflectivity are consistent with this interpretation since greater reflectivity, while implying sharp vertical gradients of temperature and salinity, does not necessarily imply stronger turbulent mixing. Instead, variations of temperature and salinity within the upper $\sim$800 m, which are associated with water masses of the Loop Current, cause strong stratification that suppresses turbulent mixing. These contrasts in temperature and salinity, together with the resultant low levels of mixing, produce semipermanent fine structure that can be seismically imaged. Closer to the continental slope, elevated mixing disturbs this fine structure, producing shorter, disrupted reflections. Beneath the thermocline, temperature and salinity values are nearly constant. Consequently, stratification is lower and mixing is enhanced. This elevated mixing further homogenizes the water mass with the consequence that seismically resolvable thermohaline fine structure is absent.

The pattern of observed mixing agrees with the findings of Wang et al. (2016), who report diapycnal diffusivities of $\sim 10^{-7}$ to 10^{-4} m^2 s^{-1} within the upper 500 m and elevated diffusivities of $\sim 10^{-7}$ to 10^{-2} m^2 s^{-1} below 1,000 m in the northern Gulf of Mexico. Qualitatively, our results also agree with those of Ledwell et al. (2016), who infer elevated diffusivities over the continental slope. However, we emphasise that our results cannot be easily quantitatively compared with those of Ledwell et al. (2016), who estimate diapycnal diffusivities of between 0.15×10^{-4} and 4×10^{-4} m^2 s^{-1} in this region. First, the results of Ledwell et al. (2016) are derived from a tracer-release experiment at a depth of $\sim$1,100 m. Wang et al. (2016) find that a layer of enhanced turbulent mixing exists at $\sim$1,100–1,300 m where $K \gtrsim 10^{-4}$ m^2 s^{-1}, which is at least 1 order of magnitude greater than that found within the upper 1,000 m.

Second, the inert tracer of Ledwell et al. (2016) was injected in July 2012 about 1 month before Hurricane Isaac crossed the northern Gulf of Mexico. A diapycnal diffusivity of $K \sim 1.3 \times 10^{-4}$ m^2 s^{-1} is estimated within the interior of the Gulf for the initial 4 months of the experiment. For the period of 4–12 months after
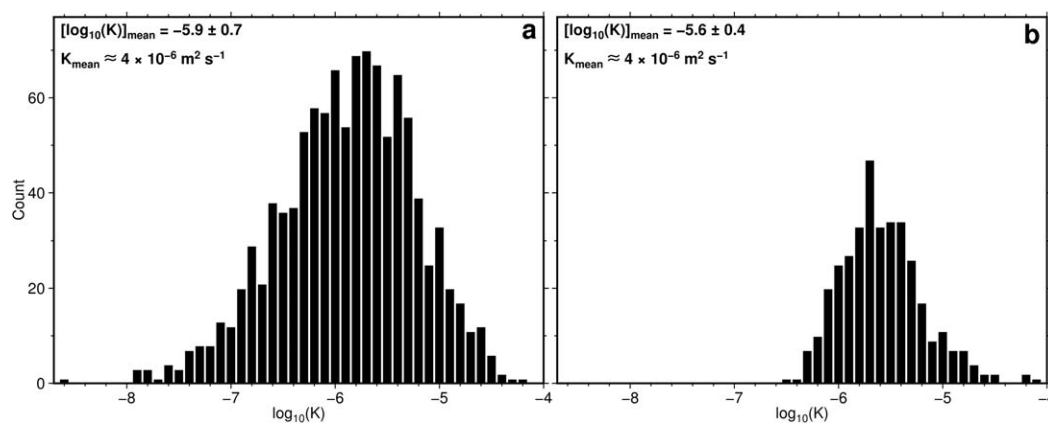

Figure 11. (a) Histogram of diapycnal diffusivities calculated from 1,078 reflections within upper 800 m of seismic image. (b) Histogram of diapycnal diffusivities within upper 800 m calculated from 75 CTD casts acquired by R/V *Pisces* between 22 August and 1 September 2010 (see Figure 1a). Note that distributions of $\log_{10}(K)$ for both data sets are approximately normal with means of $[\log_{10}(K)]_{mean} = -5.9 \pm 0.7$ and -5.6 ± 0.4 logarithmic units, respectively. In both cases, mean diffusivity, $K_{mean} \sim 4 \times 10^{-6}$ m^2 s^{-1}.
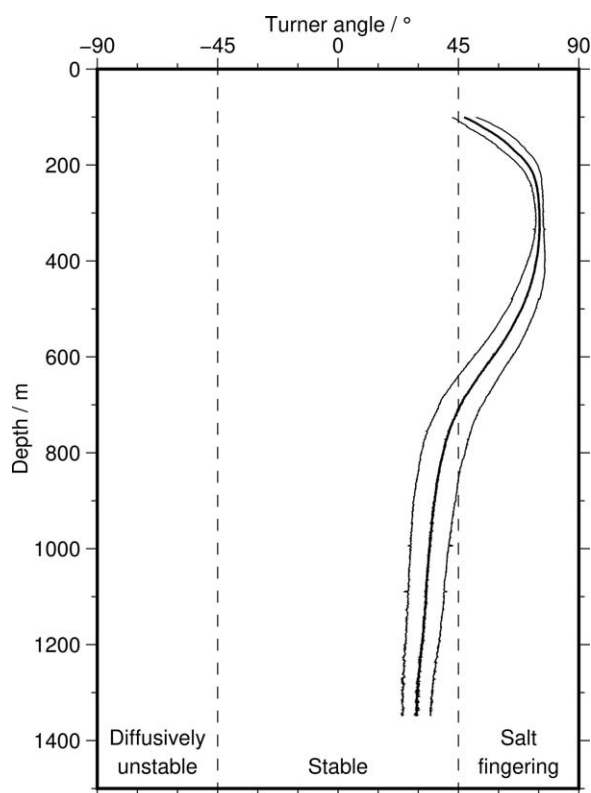
Figure 12. Average Turner angle, *Tu*, as function of depth calculated from temperature and salinity measurements for 324 CTD casts that were presmoothed using boxcar filter of length 100 m (see Figure 4). Thick/thin lines = $Tu \pm 1\sigma$; vertical dashed lines delineate diffusively unstable ($-90° < Tu < -45°$), stable ($-45° < Tu < 45°$), and salt fingering ($45° < Tu < 90°$) regimes.

injection, a lower average value of $K \sim (1.5 \pm 0.5) \times 10^{-5}$ m^2 s^{-1} is estimated. Enhanced turbulent mixing during the first 4 months is probably caused by a cascade of energy from near-inertial internal waves generated by Hurricane Isaac down to small-scale turbulent motions. Likewise, based on moored ADCP data from 2005, Jing et al. (2015) report enhanced diapycnal mixing at depths of 150–470 m in the wake of Hurricane Katrina with $K \sim 12 \times 10^{-5}$ m^2 s^{-1} which is significantly greater than the value of $K \sim 1 \times 10^{-5}$ m^2 s^{-1} obtained for the hurricane-free period of November–December 2005. Jing et al. (2015) also showed that the mean diffusivity for January 2006 increased to $K \sim 3.2 \times 10^{-5}$ m^2 s^{-1}, probably as a result of greater wind stress.

These studies and other global observations suggest that levels of mixing are strongly dependent on seasonal changes in atmospheric forcing and on the passage of energetic events such as hurricanes (e.g., Whalen et al., 2015). During the hurricane season of 2002, no hurricanes or tropical storms traversed the Gulf prior to seismic acquisition during July of that year. The seismic image thus represents a quiescent period with correspondingly low values of *K*. Prior to acquisition of hydrographic observations during 2010, Tropical Storm Bonnie crossed the Mississippi Delta and Hurricane Alex traveled through the western Gulf. The passage of these storms does not appear to have significantly elevated the diffusivities estimated from the hydrographic measurements.

Turbulent mixing within the northern Gulf thus appears to be enhanced below ∼1,000 m, probably as a result of reduced stratification. Mixing within the upper ∼1,000 m is focused predominantly above the continental shelf and slope, where impingement of mesoscale eddies on shoaling bathymetry promotes cross-shelf exchange and the development of strong currents and jets (e.g., Ohlmann & Niiler, 2005; Schmitz et al., 2005; Wang et al., 2003). The strength of turbulent mixing is also strongly dependent on seasonal changes in wind stress and on the passage of large storms.

Our results complement previous estimates of mixing concentrated near rough bathymetry, such as seamounts and mid-ocean ridges (e.g., Mauritzen et al., 2002; Polzin et al., 1997; Rudnick et al., 2003). Global compilations of dissipation rates suggest that concentration of intense near-bottom mixing within such localized regions is a general feature of the oceans (e.g., Kunze, 2017; Kunze et al., 2006; Waterhouse et al., 2014; Whalen et al., 2012). This observation is likely to have profound consequences for the quantitative understanding of global meridional circulation and has motivated McDougall and Ferrari (2017) to argue that Munk's canonical view of upwelling throughout the oceanic interior is, to some extent, misleading.

The physically reasonable spatial distribution of estimated mixing rates, and the agreement with independent analysis of CTD casts and previous work, suggests that the seismic image has faithfully recorded displacement of isopycnal surfaces by the internal wave field. This record can be used to construct accurate spatial distributions of turbulent diapycnal mixing. Exploitation of the internal wave subrange of tracked seismic reflections may thus offer a reasonable means for extracting diapycnal diffusivities from seismic images in regions where the turbulent subrange itself is not seismically resolvable. A key advantage of this technique is the potential to recover diapycnal diffusivities at increased horizontal and vertical resolutions and the ability to relate spatial patterns of diffusivity to the seismically imaged submesoscale thermohaline structure.

Finally, we note that the fine-scale parametrization exploited here accounts only for shear-induced mixing. Calculation of the Turner angle from regional CTD profiles suggests that waters within the upper ∼700 m

are unstable to double diffusive salt fingering (Figure 12). The Turner angle is a measure of the static stability of the water column and is defined by $Tu = \arctan\{-(\alpha\partial T/\partial z)/(\beta\partial S/\partial z)\} - 45°$, where α is thermal expansivity, β is haline contractivity, T is temperature, S is salinity, and z is positive downward (Ruddick, 1983). Salt fingering is a highly efficient convective mechanism for achieving diapycnal mixing that may significantly elevate values of K within the upper $\sim$700 m (Ruddick & Gargett, 2003).

6. Conclusions

We present a modified method for estimating diapycnal diffusivities from spectra of seismically imaged internal waves that builds on previous studies. Seismic images record the detailed thermohaline structure with horizontal and vertical resolutions of 5–10 m. These images faithfully record structures that are generated by the oceanic internal wave field. Our method is predicated on constructing spectra of the horizontal gradient of vertical displacement, ϕ_{ξ_x}, from automatically tracked seismic reflections. The internal wave subrange of ϕ_{ξ_x} can be isolated and compared with a reference Garrett-Munk spectrum. In this way, the diapycnal diffusivity, K, can be estimated using a fine-scale parametrization of turbulent mixing combined with the Osborn method.

We apply this approach to a seismic reflection profile that traverses the Sigsbee Escarpment on the northern margin of the Gulf of Mexico. Recovered values of K vary in a physically coherent manner over 4 orders of magnitude. This range is categorically outside the level of uncertainty in our estimates. Diffusivities are elevated over the continental slope where $K \lesssim 10^{-4}$ m^2 s^{-1}. They are suppressed by strong stratification in the upper $\sim$300 m of abyssal waters further south ($K \sim 10^{-7}$ m^2 s^{-1}). A mean diffusivity of $K \sim 4\times10^{-6}$ m^2 s^{-1} is estimated for the upper 800 m. Both this spatial variation and the mean diffusivity compare well to estimates determined from nearby CTD casts. Moreover, the enhancement of mixing above areas of rough bathymetry is in accordance with previous observations and with the recent work of McDougall and Ferrari (2017), who propose that the majority of oceanic mixing takes place in the boundary layers. We suggest that analysis of seismic images can be used to quantify changes in K within regions where no clear turbulent subrange is seismically identifiable. This novel approach would benefit from detailed comparison with values of K estimated from microstructure profiling and from fine-scale shear-strain mixing parametrizations based on vertical profiles.

Appendix A: Analysis of Seismic Image

We assume that the seismic image accurately resolves features of the internal wave field (horizontal length scales $\gtrsim$ 100 m; vertical length scales $\gtrsim$ 10 m) and that tracked reflections approximately correspond to isopycnal surfaces at these scales. Filtering of the frequency content of prestack and poststack seismic data using a variety of different band-pass filters does not significantly affect either the qualitative pattern of mixing or the recovered mean diapycnal diffusivity, K_{mean}, which lies in the range 2×10^{-6} to 4×10^{-6} m^2 s^{-1} for all filtering bands.

Horizontal power spectral densities of vertical displacement expressed in terms of two-way travel time, $\phi_\tau(k_x)$, are estimated from linearly detrended tracked reflections using a multitaper Fourier transform (Thomson, 1982). This estimation is controlled by two parameters: j_{res} (related to wave number resolution: increasing j_{res} decreases wave number resolution) and K_{res} (related to power resolution: increasing K_{res} increases power resolution). $K_{res} = 2j_{res} - 2$ represents the optimal power resolution for a given value of j_{res}. We choose $j_{res} = 4, K_{res} = 6$ as an appropriate compromise between wave number resolution and power resolution. For tracked seismic reflections of minimum length 2 km, this choice yields a minimum wave number resolution of approximately

$$j_{res}\frac{2k_N}{N} = \frac{j_{res}}{N\Delta x} = 0.002 \text{ cpm,} \tag{A1}$$

where $k_N = 0.04$ cpm is the Nyquist wave number, $N = 160$ is the number of data points for a reflection of length 2 km, and $\Delta x = 12.5$ m is the cmp spacing. The effect of parameter choice is tested by varying j_{res} and K_{res} over a range of reasonable values ($j_{res} = 3, K_{res} = 4$; $j_{res} = 4, K_{res} = 6$; $j_{res} = 5, K_{res} = 8$). Estimated values of $\log_{10}(K)$ for individual reflections vary by up to 0.7 logarithmic units, but the spatial distribution remains unaffected.

Following Percival and Walden (1993), the width of the $100(1-2p)\%$ confidence interval for $\log_{10}(\phi_\tau(k_x))$ is given by

$$\log_{10}(e)\log_{10}\left(\frac{Q_{2K_{res}}(1-p)}{Q_{2K_{res}}(p)}\right), \tag{A2}$$

where $Q_{2K_{res}}(p)$ is the pth percentage point for the χ^2 distribution with $2K_{res}$ degrees of freedom and K_{res} is the multitaper parameter described above. For $K_{res}=6$, the width of the 95% confidence interval is approximately 0.3 logarithmic units. The error in $\log_{10}(\phi_\tau(k_x))$, σ_{ϕ_τ}, is estimated to be 0.15 logarithmic units.

$\phi_\tau(k_x)$ is converted to a displacement power spectrum expressed in terms of depth, $\phi_\xi(k_x)$, by

$$\phi_\xi(k_x) = \frac{v^2}{4}\phi_\tau(k_x), \tag{A3}$$

where v is the value of a regionally averaged profile of sound speed at the average depth of the tracked reflection. The error in $\log_{10}(\phi_\xi(k_x))$, σ_{ϕ_ξ}, is given by

$$\sigma_{\phi_\xi}^2 = \sigma_{\phi_\tau}^2 + \left(2\,\log_{10}(e)\frac{\sigma_v}{v}\right)^2, \tag{A4}$$

where σ_v is the standard deviation of v. An error of ± 30 m s^{-1} in sound speed corresponds to $\frac{\sigma_v}{v}\sim 0.02$, and so errors in sound speed have an insignificant effect.

Displacement power spectra, $\phi_\xi(k_x)$, are converted to spectra of the horizontal gradient of vertical displacement, $\phi_{\xi_x}(k_x)$, using

$$\phi_{\xi_x}(k_x) = (2\pi k_x)^2 \phi_\xi(k_x), \tag{A5}$$

$$\log_{10}(\phi_{\xi_x}(k_x)) = 2\,\log_{10}(2\pi k_x) + \log_{10}(\phi_\xi(k_x)). \tag{A6}$$

Ignoring the effects of spectral leakage, the error in $\log_{10}(\phi_{\xi_x}(k_x))$ is equal to σ_{ϕ_ξ}.

We initially attempted to identify internal wave, turbulent and white noise subranges by fitting a model to each spectrum in $\log_{10}(k_x)$-$\log_{10}(\phi_{\xi_x})$ space. However, due to the onset of white noise at relatively low wave numbers, few turbulent spectral subranges were actually observed. We therefore assume that spectral amplitudes for $k_x < 10^{-2}$ cpm correspond to motions caused by the internal wave field. These low-wave-number subranges are fitted with straight lines using least squares linear regression. A standard error, $\sigma_{\hat{m}}$, on the fitted gradient, $\hat{m}$, is estimated from the covariance matrix. σ_{ϕ_ξ} is taken as the error on the individual data points. The weighted mean, $\bar{m}_w$, of the fitted gradients is given by

$$\bar{m}_w = \frac{\displaystyle\sum_{i=0}^{M}\hat{m}_i(\sigma_{\hat{m}})_i^{-2}}{\displaystyle\sum_{i=0}^{M}(\sigma_{\hat{m}})_i^{-2}}, \tag{A7}$$

where M is the total number of low-wave-number subranges. We note that there is no accepted definition of the standard error on the weighted mean, and so we quote the standard deviation of the sample as the error. As discussed in the main text, the weighted mean spectral slope of -0.2 ± 0.6 supports our assumption that the low-wave-number portions of the spectra correspond to motions caused by the internal wave field.

ϵ and K are estimated from internal wave spectral subranges using equations (3), (4), and (6). Combination of these equations shows that

$$K = K_r L(f,\bar{N})J(R_\omega)\frac{\langle\phi_{\xi_x}\rangle^2}{\langle\phi_{\xi_x}^{GM}\rangle^2}, \tag{A8}$$

where

$$K_r = \frac{\Gamma\epsilon_r}{N_r^2}, \tag{A9}$$

$$L(f,\bar{N})=\frac{f \ \text{arccosh}(\bar{N}/f)}{f_r \ \text{arccosh}(N_r/f_r)}, \tag{A10}$$

and

$$J(R_\omega)=\frac{1}{6\sqrt{2}}\frac{R_\omega(R_\omega+1)}{\sqrt{R_\omega-1}}. \tag{A11}$$

Estimated values of K have only weak explicit dependences on $\bar{N}$ and f through the term $L(f,N)$. Estimated values of K also have an implicit dependence on $\bar{N}$ through $\phi_{\xi_x}^{GM}$, which is approximately proportional to $\bar{N}^{-1}$. Uncertainty in $\bar{N}$ translates to an approximate error in $\log_{10}(K)$ of

$$\left|\frac{\partial}{\partial \bar{N}}\left[\log_{10}(L(f,\bar{N}))+2\ \log_{10}(\bar{N})\right]\right|\sigma(\bar{N}), \tag{A12}$$

$$=\log_{10}(e)\left|\frac{1}{\text{arccosh}(\bar{N}/f)}\frac{1}{f}\frac{1}{\sqrt{(\bar{N}/f)^2-1}}+\frac{2}{\bar{N}}\right|\sigma(\bar{N}), \tag{A13}$$

where vertical bars indicate that the modulus is taken and $\sigma(\bar{N})$ is the error in $\bar{N}$. We take $\bar{N}$ from a depth-dependent regionally averaged profile. Between $\sim$200 and $\sim$1,000 m depth, $\bar{N}$ varies between $\sim$4 and $\sim$1 cph. For a fixed value of $f=6.72\times10^{-5}$ rad s^{-1}, and assuming $\sigma(\bar{N})=\pm0.5$ cph, the associated error in $\log_{10}(K)$ is 0.5 logarithmic units or less. f varies between 6.54×10^{-5} and 6.9×10^{-5} rad s^{-1} along the seismic line. We use a constant value of $f=6.72\times10^{-5}$ rad s^{-1}, corresponding to the center of the seismic line. For $\bar{N}$ between 1 and 4 cph, this approximation introduces an insignificant error in $\log_{10}(K)$ of $\sim$0.01 logarithmic units.

When gauging the effect of uncertainties in R_ω and Γ, we have not formally propagated errors since the underlying distributions of R_ω and Γ are not known with sufficient accuracy. Instead, we consider the effect of choosing upper and lower bounds for R_ω and Γ on K.

We have no means to estimate R_ω, which has an average value of 7 ± 3 within the abyssal ocean (Kunze et al., 2006). It is plausible that R_ω varies systematically when water depth shallows toward the continental slope. Even if R_ω varies between 2 and 20, the assumption of a constant value of $R_\omega=7$ yields an uncertainty in $\log_{10}(K)$ of $<$0.6 logarithmic units as shown by

$$\log_{10}(K)=\log_{10}\left(6\sqrt{2}J(R_\omega)\right)+A, \tag{A14}$$

$$=\log_{10}\left(\frac{R_\omega(R_\omega+1)}{\sqrt{R_\omega-1}}\right)+A, \tag{A15}$$

$$\approx 0.8+A \ \text{for} \ R_\omega=2, \tag{A16}$$

$$\approx 1.4+A \ \text{for} \ R_\omega=7, \tag{A17}$$

$$\approx 2.0+A \ \text{for} \ R_\omega=20, \tag{A18}$$

where A includes all terms independent of R_ω. To account for all the observed spatial variation in $\log_{10}(K)$, R_ω would have to vary over 3 orders of magnitude.

Finally, Γ is probably not constant but is likely to vary both temporally and spatially (Mashayek et al., 2017). Taking lower and upper bounds of $\Gamma \sim 0.1$ and $\Gamma \sim 0.4$, respectively, implies that assumption of a constant value of $\Gamma=0.2$ introduces an uncertainty in $\log_{10}(K)$ of up to 0.3 logarithmic units as shown by

$$\log_{10}(K)=\log_{10}(\Gamma)+B, \tag{A19}$$

$$=-1+B \ \text{for} \ \Gamma=0.1, \tag{A20}$$

$$\approx -0.7+B \ \text{for} \ \Gamma=0.2, \tag{A21}$$

$$\approx -0.4+B \ \text{for} \ \Gamma=0.4, \tag{A22}$$

where B includes all terms independent of Γ. We also note that a constant flux Richardson number, R_f, of 0.17 is assumed in estimation of $\epsilon_r=7.2\times10^{-10}$ m^2 s^{-1}.
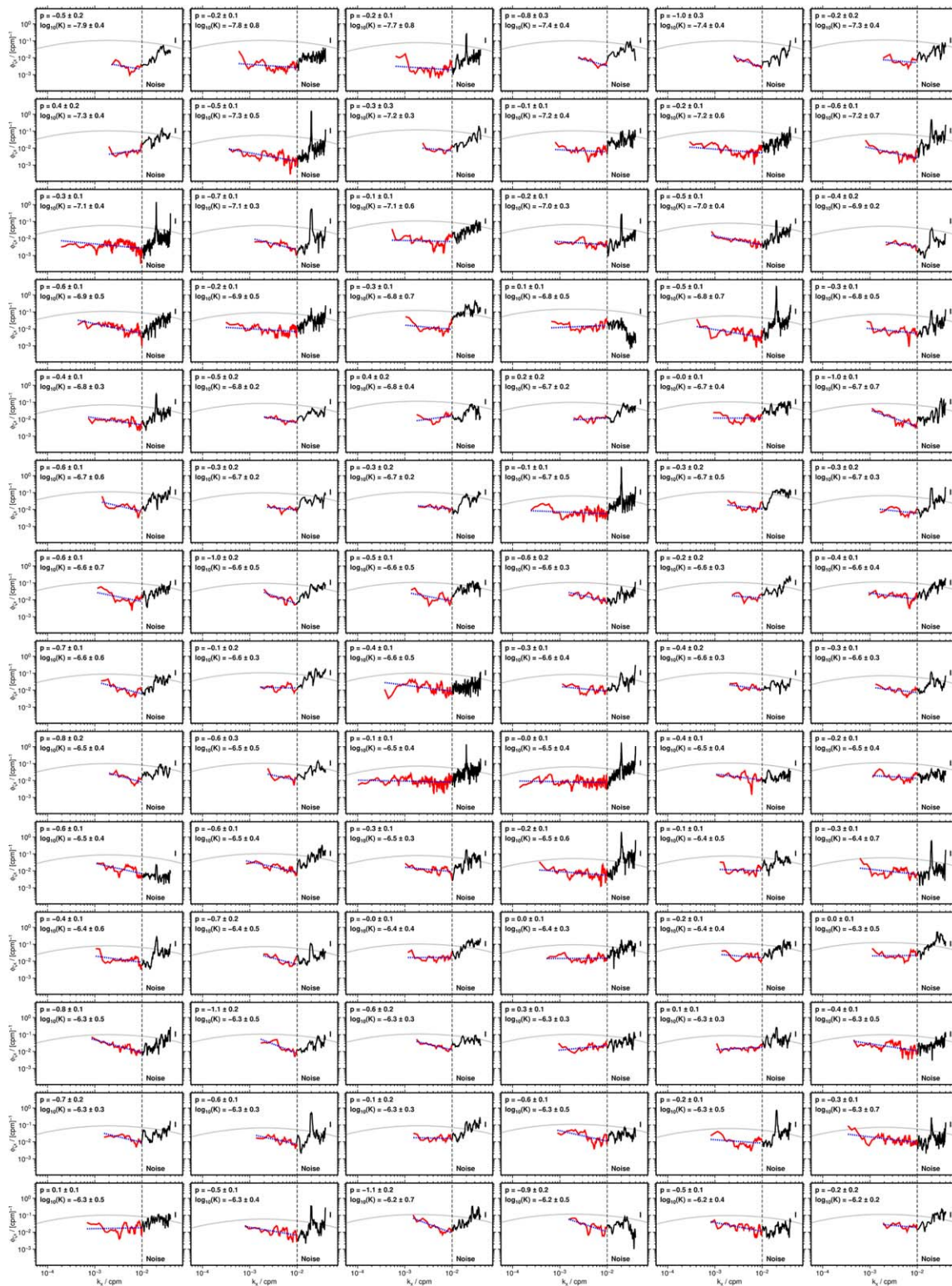
Figure A1. Suite of 336 horizontal gradient spectra calculated from tracked seismic reflections. Black/red lines = observed spectra with identified internal wave subranges; vertical dashed line = white noise cutoff at $k_x = 0.01$ cpm determined by direct data transform; blue dotted line = best fit straight line with gradient of p for internal wave subrange; gray line = GM76 reference spectrum; vertical black line on right-hand side = 95% confidence interval for ϕ_{ζ_x}, centered on $\phi_{\zeta_x} = 10^{-1}$ (cpm)$^{-1}$ and calculated using method of Percival and Walden (1993). Optimal value of p and calculated value of $\log_{10}(K)$ shown in top left-hand corner. Quoted uncertainties for $\log_{10}(K)$ are solely based on standard deviation of $\left(\phi_{\zeta_x} / \phi_{\zeta_x}^{GM} \right)$ for internal wave subrange. Spectra are ordered such that energy increases from top left to bottom right.
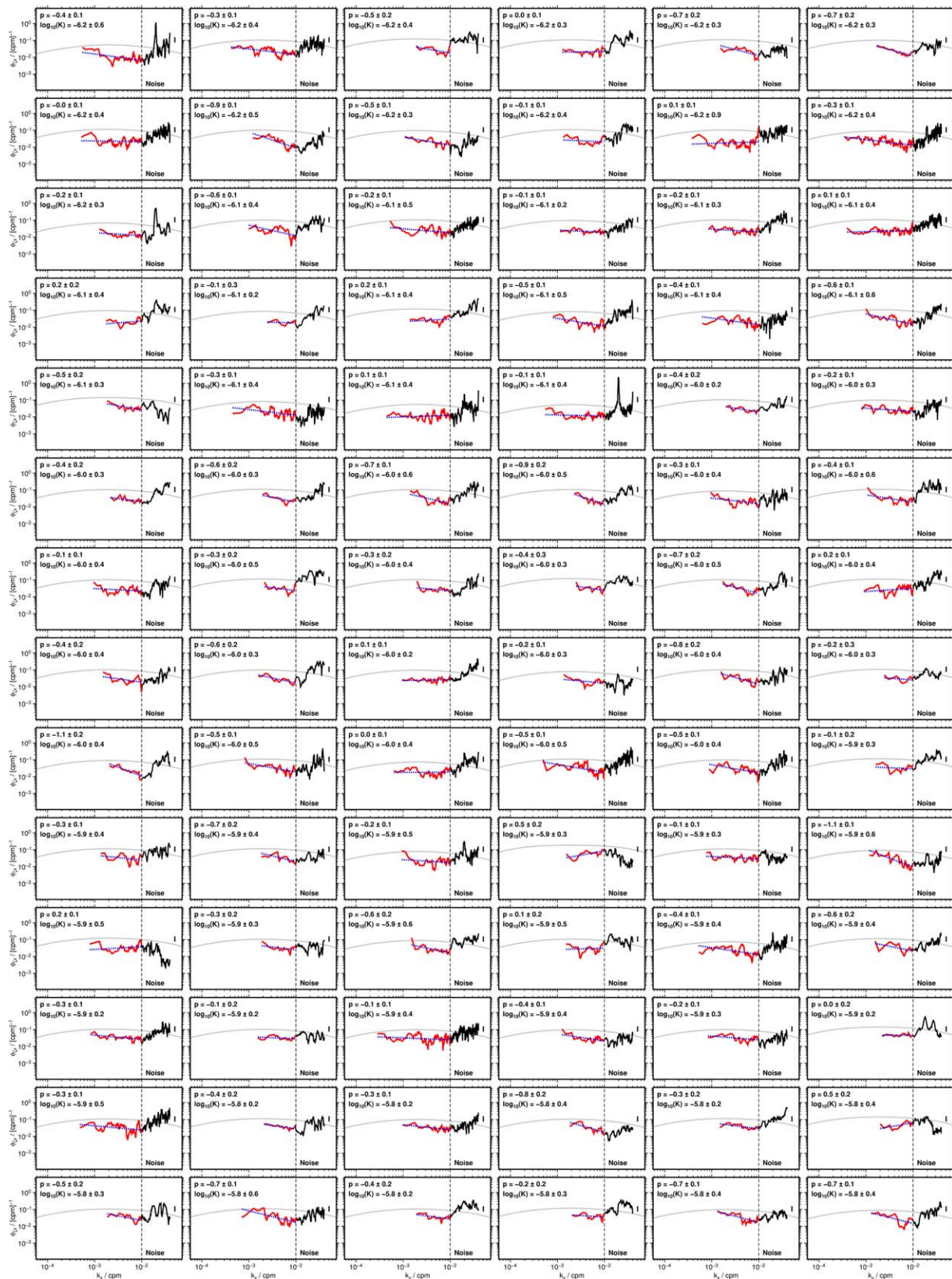
Figure A1. (continued)
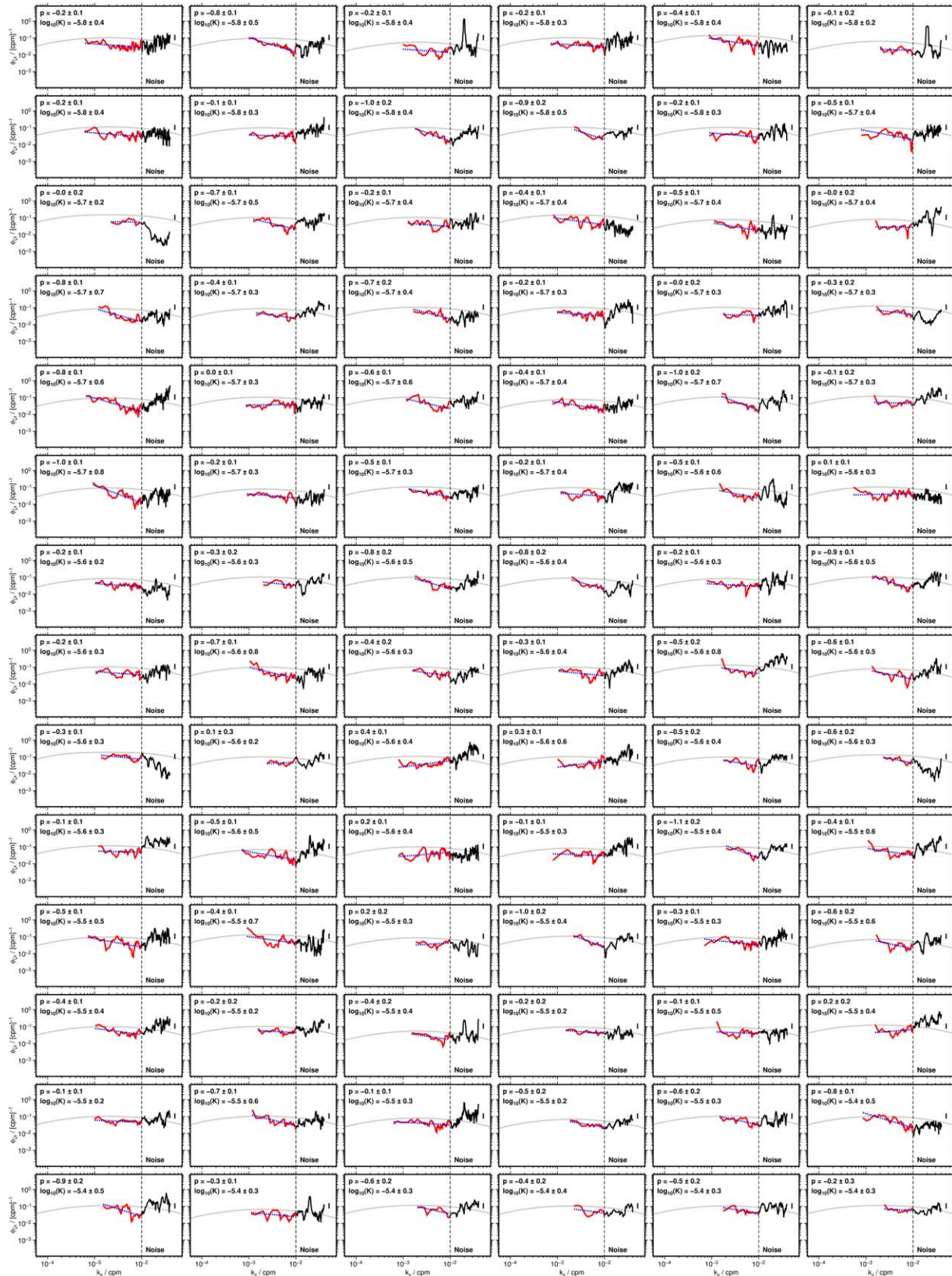
Figure A1. (continued)
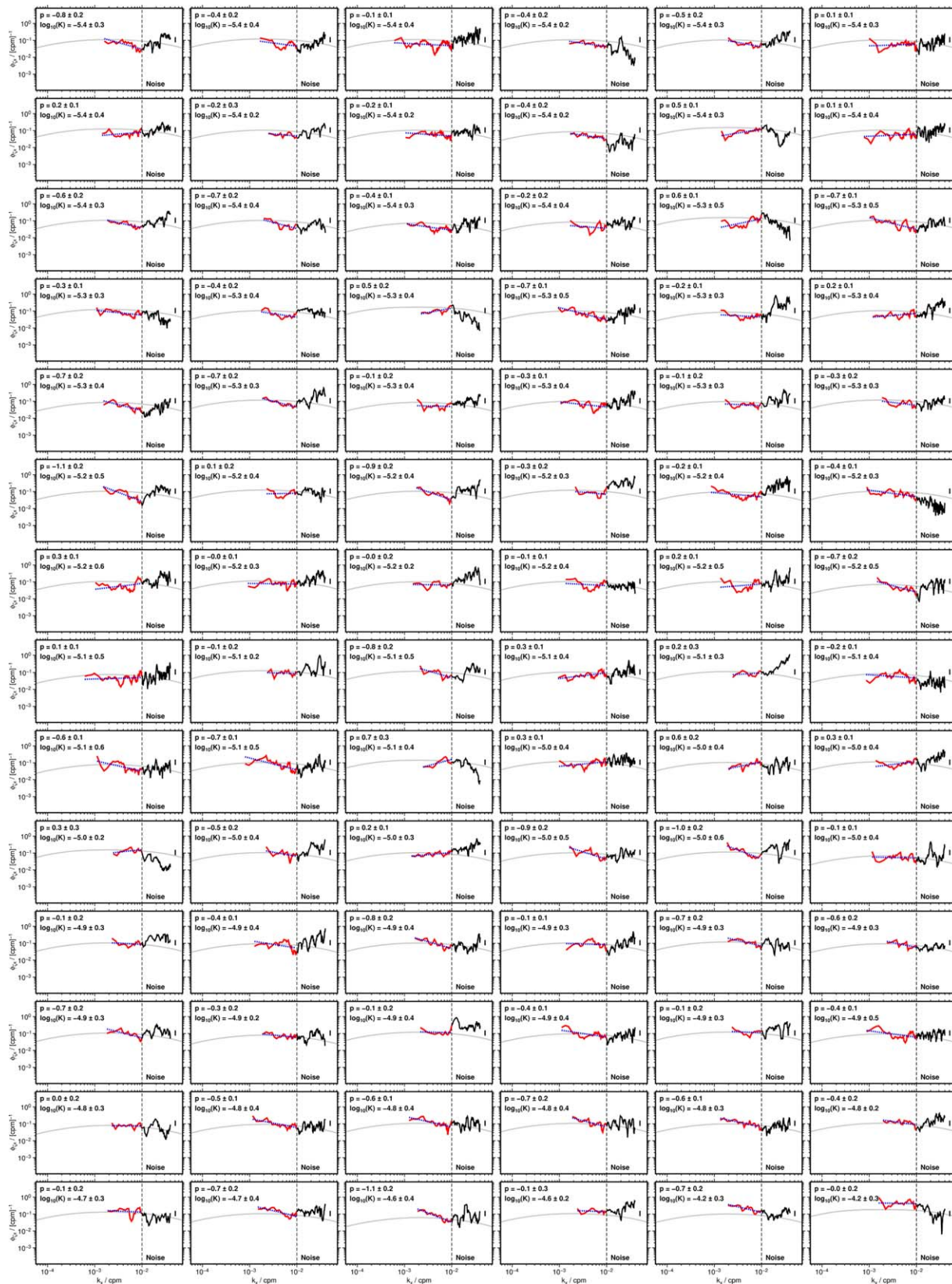
Figure A1. (continued)

Uncertainties in R_ω, $\bar{N}$, f, and Γ are therefore insufficient to account for the variation of K recovered across the seismic image (10^{-8} m^2 s$^{-1} \lesssim K \lesssim 10^{-4}$ m^2 s^{-1}).

Error in the energy level ratio of individual spectra is estimated as the standard deviation of the ratio

$$\frac{\phi_{\xi_x}}{\phi_{\xi_x}^{GM}} \tag{A23}$$

over the range of integration for k_x. Corresponding uncertainties in $\log_{10}(K)$ range from 0.13 to 1.6 logarithmic units (the mean uncertainty is 0.5 ± 0.2 logarithmic units).

Example spectra and corresponding values of p and K are given in Figure A1.

A histogram of estimated values of $\log_{10}(K)$ for the upper 800 m suggests a normal distribution with a mean of $[\log_{10}(K)]_{mean} = -5.9 \pm 0.7$ logarithmic units (Figure 11a). The distribution of K is therefore approximately lognormal. K_{mean} is estimated using

$$K_{mean} = \exp\left[\frac{\mu}{\log_{10}(e)} + \frac{1}{2}\left(\frac{\sigma}{\log_{10}(e)}\right)^2\right], \tag{A24}$$

where $\mu = [\log_{10}(K)]_{mean}$ and σ^2 are the mean and variance of $\log_{10}(K)$, respectively. K_{mean} is estimated to be $\sim 4 \times 10^{-6}$ m^2 s^{-1}.

Estimated values of $\log_{10}(K)$ show a slight negative correlation with the length of tracked reflections ($r = -0.24$). We investigate this effect by dividing tracked reflections greater than 4 km in length into multiple segments of length 2–4 km. The pattern of mixing estimated from these subdivided tracks is comparable to that presented above. Therefore, we believe that the negative correlation of $\log_{10}(K)$ and reflection length is a physical effect. In regions of low mixing, semipermanent fine structure is manifest as long, continuous reflections. In regions of higher mixing, fine structure is disrupted and reflections are consequently shorter and more discontinuous.

Appendix B: Analysis of Hydrographic Casts

Erroneous values of temperature and salinity are removed following NOAA guidelines for the Deepwater Horizon program (https://data.nodc.noaa.gov/DeepwaterHorizon). Profiles are divided into blocks of 100 values. Values of temperature or salinity that lie more than two standard deviations away from the mean of these 100 values are removed. This process is repeated with a threshold of 20 standard deviations to yield corrected profiles.

We assume that computation of buoyancy frequency and strain from profiles of temperature and salinity is accurate. Variation of multitaper transform parameters, as described in Appendix A, used for calculation of strain spectra yields variation in individual values of $\log_{10}(K)$ of <0.5 logarithmic units. Uncertainties in R_ω and Γ affect estimates of $\log_{10}(K)$ as discussed in Appendix A. The error in the energy level ratio of individual spectra is estimated as the standard deviation of the ratio

$$\frac{\phi_{\xi_z}}{\phi_{\xi_z}^{GM}} \tag{B1}$$

over the k_z range of integration. Corresponding uncertainties in $\log_{10}(K)$ range from 0.09 to 2.2 logarithmic units (mean uncertainty is 0.29 ± 0.13 logarithmic units).

A histogram of estimated values of $\log_{10}(K)$ for the upper 800 m suggests a normal distribution with a mean of $[\log_{10}(K)]_{mean} = -5.6 \pm 0.4$ logarithmic units (Figure 11a). The distribution of K is therefore approximately lognormal. The expectation value of K, K_{mean}, is estimated using

$$K_{mean} = \exp\left[\frac{\mu}{\log_{10}(e)} + \frac{1}{2}\left(\frac{\sigma}{\log_{10}(e)}\right)^2\right], \tag{B2}$$

where $\mu = [\log_{10}(K)]_{mean}$ and σ^2 are the mean and variance of $\log_{10}(K)$, respectively. K_{mean} is estimated to be $\sim 4 \times 10^{-6}$ m^2 s^{-1}.

References

Barnes, A. E. (2007). A tutorial on complex seismic trace analysis. *Geophysics*, *72*(6), W33–W43. https://doi.org/10.1190/1.2785048

Batchelor, G. K. (1959). Small-scale variation of convected quantities like temperature in turbulent fluid. Part 1: General discussion and the case of small conductivity. *Journal of Fluid Mechanics*, *5*(1), 113–133. https://doi.org/10.1017/S002211205900009X

Bell, T. H. (1976). The structure of internal wave spectra as determined from towed thermistor chain measurements. *Journal of Geophysical Research*, *81*(21), 3709–3714. https://doi.org/10.1029/JC081i021p03709

Biescas, B., Ruddick, B. R., Nedimovic, M. R., Sallarès, V., Bornstein, G., & Mojica, J. F. (2014). Recovery of temperature, salinity, and potential density from ocean reflectivity. *Journal of Geophysical Research: Oceans*, *119*, 3171–3184. https://doi.org/10.1002/2013JC009662

Bray, N. A., & Fofonoff, N. P. (1981). Available potential energy for MODE eddies. *Journal of Physical Oceanography*, *11*(1), 30–47. https://doi.org/10.1175/1520-0485(1981)011<0030:APEFME>2.0.CO;2

Cairns, J. L., & Williams G. O. (1976). Internal wave observations from a midwater float 2. *Journal of Geophysical Research*, *81*(12), 1943–1950. https://doi.org/10.1029/JC081i012p01943

Carter, G. S., Gregg, M. C., & Lien, R.-C. (2005). Internal waves, solitary-like waves, and mixing on the Monterey Bay shelf. *Continental Shelf Research*, *25*(12), 1499–1520. https://doi.org/10.1016/j.csr.2005.04.011

Corrsin, S. (1951). On the spectrum of isotropic temperature fluctuations in an isotropic turbulence. *Journal of Applied Physics*, *22*(4), 469–473. https://doi.org/10.1063/1.1699986

Ewart, T. E. (1976). Observations from straight line isobaric runs of SPURV. In *Proceedings of the IAPSO/IAMAP PSII* (pp. 1–18). Edinburgh, UK: Joint Oceanographic Assembly.

Falder, M., White, N. J., & Caulfield, C. P. (2016). Seismic imaging of rapid onset of stratified turbulence in the South Atlantic Ocean. *Journal of Physical Oceanography*, *46*(4), 1023–1044. https://doi.org/10.1175/JPO-D-15-0140.1

Fer, I. (2006). Scaling turbulent dissipation in an Arctic fjord. *Deep Sea Research, Part II: Topical Studies in Oceanography*, *53*(1), 77–95. https://doi.org/10.1016/j.dsr2.2006.01.003

Fer, I., Nandi, P., Holbrook, W. S., Schmitt, R. W., & Páramo, P. (2010). Seismic imaging of a thermohaline staircase in the western tropical North Atlantic. *Ocean Science*, *6*, 621–631. https://doi.org/10.5194/os-6-621-2010

Ferrari, R., & Wunsch, C. (2009). Ocean circulation kinetic energy: Reservoirs, sources, and sinks. *Annual Review of Fluid Mechanics*, *41*(1), 253–282. https://doi.org/10.1146/annurev.fluid.40.111406.102139

Fortin, W. F. J., & Holbrook, W. S. (2009). Sound speed requirements for optimal imaging of seismic oceanography data. *Geophysical Research Letters*, *36*, L00D01. https://doi.org/10.1029/2009GL038991

Fortin, W. F. J., Holbrook, W. S., & Schmitt, R. W. (2016). Mapping turbulent diffusivity associated with oceanic internal lee waves offshore Costa Rica. *Ocean Science*, *12*(4), 601–612. https://doi.org/10.5194/os-12-601-2016

Frants, M., Damerell, G. M., Gille, S. T., Heywood, K. J., MacKinnon, J., & Sprintall, J. (2013). An assessment of density-based finescale methods for estimating diapycnal diffusivity in the Southern Ocean. *Journal of Atmospheric and Oceanic Technology*, *30*(11), 2647–2661. https://doi.org/10.1175/JTECH-D-12-00241.1

Gargett, A. E., & Holloway, G. (1984). Dissipation and diffusion by internal wave breaking. *Journal of Marine Research*, *42*(1), 15–27. https://doi.org/10.1357/002224084788506158

Garrett, C., & Munk, W. (1972). Space-time scales of internal waves. *Geophysical Fluid Dynamics*, *2*(1), 225–264. https://doi.org/10.1080/03091927208236082

Garrett, C., & Munk, W. (1975). Space-time scales of internal waves: A progress report. *Journal of Geophysical Research*, *80*(3), 291–297. https://doi.org/10.1029/JC080i003p00291

Gregg, M. C. (1989). Scaling turbulent dissipation in the thermocline. *Journal of Geophysical Research*, *94*(C7), 9686–9698. https://doi.org/10.1029/JC094iC07p09686

Gregg, M. C., & Kunze, E. (1991). Shear and strain in Santa Monica Basin. *Journal of Geophysical Research*, *96*(C9), 16709–16719. https://doi.org/10.1029/91JC01385

Gregg, M. C., Sanford, T. B., & Winkel, D. P. (2003). Reduced mixing from the breaking of internal waves in equatorial waters. *Nature*, *422*(6931), 513–515. https://doi.org/10.1038/nature01507

Henyey, F. S., Wright, J., & Flatté, S. M. (1986). Energy and action flow through the internal wave field: An Eikonal approach. *Journal of Geophysical Research*, *91*(C7), 8487–8495. https://doi.org/10.1029/JC091iC07p08487

Holbrook, W. S., & Fer, I. (2005). Ocean internal wave spectra inferred from seismic reflection transects. *Geophysical Research Letters*, *32*,L15604. https://doi.org/10.1029/2005GL023733

Holbrook, W. S., Fer, I., Schmitt, R. W., Lizarralde, D., Klymak, J. M., Helfrich, L. C., & Kubichek, R. (2013). Estimating oceanic turbulence dissipation from seismic images. *Journal of Atmospheric and Oceanic Technology*, *30*(8), 1767–1788. https://doi.org/10.1175/JTECH-D-12-00140.1

Holbrook, W. S., Páramo, P., Pearse, S., & Schmitt, R. W. (2003). Thermohaline fine structure in an oceanographic front from seismic reflection profiling. *Science*, *301*(5634), 821–824. https://doi.org/10.1126/science.1085116

Ivey, G. N., Winters, K. B., & Koseff, J. R. (2008). Density stratification, turbulence, but how much mixing? *Annual Review of Fluid Mechanics*, *40*, 169–184. https://doi.org/10.1146/annurev.fluid.39.050905.110314

Jing, Z., Chang, P., DiMarco, S. F., & Wu, L. (2015). Role of near-inertial internal waves in subthermocline diapycnal mixing in the northern Gulf of Mexico. *Journal of Physical Oceanography*, *45*(12), 3137–3154. https://doi.org/10.1175/JPO-D-14-0227.1

Katz, E. J. (1973). Profile of an isopycnal surface in the main thermocline of the Sargasso Sea. *Journal of Physical Oceanography*, *3*(4), 448–457. https://doi.org/10.1175/1520-0485(1973)003<0448:POAISI>2.0.CO;2

Katz, E. J., & Briscoe, M. G. (1979). Vertical coherence of the internal wave field from towed sensors. *Journal of Physical Oceanography*, *9*(3), 518–530.

Klaeschen, D., Hobbs, R. W., Krahmann, G., Papenberg, C., & Vsemirnova, E. (2009). Estimating movement of reflectors in the water column using seismic oceanography. *Geophysical Research Letters*, *36*, L00D03. https://doi.org/10.1029/2009GL038973

Klymak, J. M., & Moum, J. N. (2007). Oceanic isopycnal slope spectra. Part I: Internal waves. *Journal of Physical Oceanography*, *37*(5), 1215–1231. https://doi.org/10.1175/JPO3073.1

Kolmogorov, A. N. (1941). The local structure of turbulence in incompressible viscous fluid for very large Reynolds numbers. *Doklady Akademii Nauk SSSR*, *30*, 301–305.

Krahmann, G., Brandt, P., Klaeschen, D., & Reston, T. (2008). Mid-depth internal wave energy off the Iberian Peninsula estimated from seismic reflection data. *Journal of Geophysical Research*, *113*, C12016. https://doi.org/10.1029/2007JC004678

Krahmann, G., Papenberg, C., Brandt, P., & Vogt, M. (2009). Evaluation of seismic reflector slopes with a Yoyo-CTD. *Geophysical Research Letters*, *36*, L00D02. https://doi.org/10.1029/2009GL038964

Kunze, E. (2017). Internal-wave-driven mixing: Global geography and budgets. *Journal of Physical Oceanography*, *47*(6), 1325–1345. https://doi.org/10.1175/JPO-D-16-0141.1

Kunze, E., Firing, E., Hummon, J. M., Chereskin, T. K., & Thurnherr, A. M. (2006). Global abyssal mixing inferred from lowered ADCP shear and CTD strain profiles. *Journal of Physical Oceanography*, *36*(8), 1553–1576. https://doi.org/10.1175/JPO2926.1

Ledwell, J. R., He, R., Xue, Z., Dimarco, S. F., Spencer, L. J., & Chapman, P. (2016). Dispersion of a tracer in the deep Gulf of Mexico. *Journal of Geophysical Research: Oceans*, *121*, 1110–1132. https://doi.org/10.1002/2015JC011405

Ledwell, J. R., Montgomery, E. T., Polzin, K. L., St. Laurent, L. C., Schmitt, R. W., & Toole, J. M. (2000). Evidence for enhanced mixing over rough topography in the abyssal ocean. *Nature*, *403*(6766), 179–182. https://doi.org/10.1038/35003164

Ledwell, J. R., Watson, A. J., & Law, C. S. (1998). Mixing of a tracer in the pycnocline. *Journal of Geophysical Research*, *103*(C10), 21499–21529. https://doi.org/10.1029/98JC01738

Lee, C. M., Kunze, E., Sanford, T. B., Nash, J. D., Merrifield, M. A., & Holloway, P. E. (2006). Internal tides and turbulence along the 3000-m isobath of the Hawaiian Ridge. *Journal of Physical Oceanography*, *36*(6), 1165–1183. https://doi.org/10.1175/JPO2886.1

MacKinnon, J. A., & Gregg, M. C. (2003). Mixing on the late-summer New England Shelf—Solibores, shear, and stratification. *Journal of Physical Oceanography*, *33*(7), 1476–1492. https://doi.org/10.1175/1520-0485(2003)033<1476:MOTLNE>2.0.CO;2

Mashayek, A., Caulfield, C. P., & Peltier, W. R. (2013). Time-dependent, non-monotonic mixing in stratified turbulent shear flows: Implications for oceanographic estimates of buoyancy flux. *Journal of Fluid Mechanics*, *736*, 570–593. https://doi.org/10.1017/jfm.2013.551

Mashayek, A., Salehipour, H., Bouffard, D., Caulfield, C. P., Ferrari, R., Nikurashin, M., . . . Smyth, W. D. (2017). Efficiency of turbulent mixing in the abyssal ocean circulation. *Geophysical Research Letters*, *44*, 6296–6306. https://doi.org/10.1002/2016GL072452

Mauritzen, C., Polzin, K. L., McCartney, M. S., Millard, R. C., & West-Mack, D. E. (2002). Evidence in hydrography and density fine structure for enhanced vertical mixing over the Mid-Atlantic Ridge in the western Atlantic. *Journal of Geophysical Research*, *107*(C10), 3147. https://doi.org/10.1029/2001JC001114

McComas, C. H., & Müller, P. (1981). The dynamic balance of internal waves. *Journal of Physical Oceanography*, *11*(7), 970–986. https://doi.org/10.1175/1520-0485(1981)011<0970:TDBOIW>2.0.CO;2

McDougall, T. J., & Ferrari, R. (2017). Abyssal upwelling and downwelling driven by near-boundary mixing. *Journal of Physical Oceanography*, *47*(2), 261–283. https://doi.org/10.1175/JPO-D-16-0082.1

McKean, R. S., & Ewart, T. E. (1974). Temperature spectra in the deep ocean off Hawaii. *Journal of Physical Oceanography*, *4*(2), 191–199. https://doi.org/10.1175/1520-0485(1974)004<0191:TSITDO>2.0.CO;2

Montgomery, R. B. (1939). Ein Versuch, den vertikalen und seitlichen Austausch in der Tiefe der Sprungschicht im äquatorialen Atlantischen Ozean zu bestimmen. *Annalen der Hydrographie und maritimen Meteorologie*, *67*, 242–246.

Müller, P., Olbers, D. J., & Willebrand, J. (1978). The Iwex spectrum. *Journal of Geophysical Research*, *83*(C1), 479–500. https://doi.org/10.1029/JC083iC01p00479

Munk, W. (1981). Internal waves and small-scale processes. In B. A. Warren & C. Wunsch (Eds.), *Evolution of physical oceanography: Scientific surveys in honor of Henry Stommel* (chap. 9, pp. 264–291). Cambridge, MA: MIT Press.

Munk, W. H. (1966). Abyssal recipes. *Deep Sea Research and Oceanographic Abstracts*, *13*(4), 707–730. https://doi.org/10.1016/0011-7471(66)90602-4

Nakamura, Y., Noguchi, T., Tsuji, T., Itoh, S., Niino, H., & Matsuoka, T. (2006). Simultaneous seismic reflection and physical oceanographic observations of oceanic fine structure in the Kuroshio extension front. *Geophysical Research Letters*, *33*, L23605. https://doi.org/10.1029/2006GL027437

Nandi, P., Holbrook, W. S., Pearse, S., Páramo, P., & Schmitt, R. W. (2004). Seismic reflection imaging of water mass boundaries in the Norwegian Sea. *Geophysical Research Letters*, *31*, L23311. https://doi.org/10.1029/2004GL021325

Nash, J. D., Kunze, E., Toole, J. M., & Schmitt, R. W. (2004). Internal tide reflection and turbulent mixing on the continental slope. *Journal of Physical Oceanography*, *34*(5), 1117–1134. https://doi.org/10.1175/1520-0485(2004)034<1117:ITRATM>2.0.CO;2

Nastrom, G. D., & Gage, K. S. (1985). A climatology of atmospheric wavenumber spectra of wind and temperature observed by commercial aircraft. *Journal of the Atmospheric Sciences*, *42*(9), 950–960. https://doi.org/10.1175/1520-0469(1985)042<0950:ACOAWS>2.0.CO;2

Naveira Garabato, A. C., Oliver, K. I. C., Watson, A. J., & Messias, M.-J. (2004). Turbulent diapycnal mixing in the Nordic seas. *Journal of Geophysical Research*, *109*, C12010. https://doi.org/10.1029/2004JC002411

Nowlin, W. D. J., Jochens, A. E., DiMarco, S. F., Reid, R. O., & Howard, M. K. (2001). *Deepwater physical oceanography reanalysis and synthesis of historical data: Synthesis report* (Tech. Rep. OCS Study MMS 2001-064). New Orleans, LA: US Department of the Interior, Minerals Management Service, Gulf of Mexico OCS Region.

Obukhov, A. M. (1949). The structure of the temperature field in a turbulent flow. *Izvestiya Akademii Nauk SSR, Seriya Geograficheskaya i Geofizicheskaya*, *13*, 58–69.

Ohlmann, J. C., & Niiler, P. P. (2005). Circulation over the continental shelf in the northern Gulf of Mexico. *Progress in Oceanography*, *64*(1), 45–81. https://doi.org/10.1016/j.pocean.2005.02.001

Osborn, T. (1980). Estimates of the local rate of vertical diffusion from dissipation measurements. *Journal of Physical Oceanography*, *10*(1), 83–89. https://doi.org/10.1175/1520-0485(1980)010<0083:EOTLRO>2.0.CO;2

Osborn, T. R., & Cox, C. S. (1972). Oceanic fine structure. *Geophysical Fluid Dynamics*, *3*(1), 321–345. https://doi.org/10.1080/03091927208236085

Ozmidov, R. V. (1965). On the turbulent exchange in a stably stratified ocean. *Izvestiya of the Academy of Sciences of the USSR, Atmospheric and Oceanic Physics*, *1*(8), 853–860.

Percival, D. B., & Walden, A. T. (1993). *Spectral analysis for physical applications: Multitaper and conventional univariate techniques* (583 pp.). Cambridge, UK: Cambridge University Press.

Pinheiro, L. M., Song, H., Ruddick, B., Dubert, J., Ambar, I., Mustafa, K., & Bezerra, R. (2010). Detailed 2-D imaging of the Mediterranean outflow and meddies off W Iberia from multichannel seismic data. *Journal of Marine Systems*, *79*(1), 89–100. https://doi.org/10.1016/j.jmarsys.2009.07.004

Polzin, K. L., Naveira Garabato, A. C., Huussen, T. N., Sloyan, B. M., & Waterman, S. (2014). Finescale parameterizations of turbulent dissipation. *Journal of Geophysical Research: Oceans*, *119*, 1383–1419. https://doi.org/10.1002/2013JC008979

Polzin, K. L., Toole, J. M., Ledwell, J. R., & Schmitt, R. W. (1997). Spatial variability of turbulent mixing in the Abyssal Ocean. *Science*, *276*(5309), 93–96. https://doi.org/10.1126/science.276.5309.93

Polzin, K. L., Toole, J. M., & Schmitt, R. W. (1995). Finescale parameterizations of turbulent dissipation. *Journal of Physical Oceanography*, *25*(3), 306–328. https://doi.org/10.1175/1520-0485(1995)025<0306:FPOTD>2.0.CO;2

Riley, J. J., & Lindborg, E. (2008). Stratified turbulence: A possible interpretation of some geophysical turbulence measurements. *Journal of the Atmospheric Sciences*, *65*(7), 2416–2424. https://doi.org/10.1175/2007JAS2455.1

Rivas, D., Badan, A., & Ochoa, J. (2005). The ventilation of the deep Gulf of Mexico. *Journal of Physical Oceanography*, *35*(10), 1763–1781. https://doi.org/10.1175/JPO2786.1

Ruddick, B. (1983). A practical indicator of the stability of the water column to double-diffusive activity. *Deep Sea Research, Part A: Oceanographic Research Papers*, *30*(10), 1105–1107. https://doi.org/10.1016/0198-0149(83)90063-8

Ruddick, B., & Gargett, A. E. (2003). Oceanic double-infusion: Introduction. *Progress in Oceanography*, *56*(3–4), 381–393. https://doi.org/10.1016/S0079-6611(03)00024-7

Rudnick, D. L., Boyd, T. J., Brainard, R. E., Carter, G. S., Egbert, G. D., Gregg, M. C., . . . Sanford, T. B. (2003). From tides to mixing along the Hawaiian Ridge. *Science*, *301*(5631), 355–357. https://doi.org/10.1126/science.1085837

Sallarès, V., Biescas, B., Buffett, G., Carbonell, R., Dañobeitia, J. J., & Pelegrí, J. L. (2009). Relative contribution of temperature and salinity to ocean acoustic reflectivity. *Geophysical Research Letters*, *36*, L00D06. https://doi.org/10.1029/2009GL040187

Schmitz, W. J., Biggs, D., Lugo-Fernandez, C. A., Oey, L.-Y., & Sturges, W. (2005). A synopsis of the circulation in the Gulf of Mexico and on its continental margins. In W. Sturges & A. Lugo-Fernandez (Eds.), *Circulation in the Gulf of Mexico: Observations and models* (chap. 2, pp. 11–29). Washington, DC: American Geophysical Union.

Sheen, K. L., White, N., Caulfield, C. P., & Hobbs, R. W. (2011). Estimating geostrophic shear from seismic images of oceanic structure. *Journal of Atmospheric and Oceanic Technology*, *28*(9), 1149–1154. https://doi.org/10.1175/JTECH-D-10-05012.1

Sheen, K. L., White, N. J., & Hobbs, R. W. (2009). Estimating mixing rates from seismic images of oceanic structure. *Geophysical Research Letters*, *36*, L00D04. https://doi.org/10.1029/2009GL040106

Stolt, R. H. (1978). Migration by Fourier transform. *Geophysics*, *43*(1), 23–48. https://doi.org/10.1190/1.1440826

Sturges, W., Lugo-Fernandez, A., & Shargel, M. D. (2005). Introduction to circulation in the Gulf of Mexico. In W. Sturges & A. Lugo-Fernandez (Eds.), *Circulation in the Gulf of Mexico: Observations and models* (chap. 1, pp. 1–10). Washington, DC: American Geophysical Union. https://doi.org/10.1029/161GM02

Thomson, D. J. (1982). Spectrum estimation and harmonic analysis. *Proceedings of the IEEE*, *70*, 1055–1096. https://doi.org/10.1109/PROC.1982.12433

Toole, J. M., Schmitt, R. W., & Polzin, K. L. (1994). Estimates of diapycnal mixing in the Abyssal Ocean. *Science*, *264*(5162), 1120–1123. https://doi.org/10.1126/science.264.5162.1120

Vsemirnova, E., Hobbs, R., Serra, N., Klaeschen, D., & Quentel, E. (2009). Estimating internal wave spectra using constrained models of the dynamic ocean. *Geophysical Research Letters*, *36*, L00D07. https://doi.org/10.1029/2009GL039598

Wang, D.-P., Oey, L.-Y., Ezer, T., & Hamilton, P. (2003). Near-surface currents in DeSoto Canyon (1997–99): Comparison of current meters, satellite observation, and model simulation. *Journal of Physical Oceanography*, *33*(1), 313–326. https://doi.org/10.1175/1520-0485(2003)033<0313:NSCIDC>2.0.CO;2

Wang, Z., DiMarco, S. F., & Socolofsky, S. A. (2016). Turbulence measurements in the northern Gulf of Mexico: Application to the Deepwater Horizon oil spill on droplet dynamics. *Deep Sea Research, Part I: Oceanographic Research Papers*, *109*, 40–50. https://doi.org/10.1016/j.dsr.2015.12.013

Waterhouse, A. F., MacKinnon, J. A., Nash, J. D., Alford, M. H., Kunze, E., Simmons, H. L., . . . Lee, C. M. (2014). Global patterns of diapycnal mixing from measurements of the turbulent dissipation rate. *Journal of Physical Oceanography*, *44*(7), 1854–1872. https://doi.org/10.1175/JPO-D-13-0104.1

Whalen, C. B., MacKinnon, J. A., Talley, L. D., & Waterhouse, A. F. (2015). Estimating the mean diapycnal mixing using a finescale strain parameterization. *Journal of Physical Oceanography*, *45*(4), 1174–1188. https://doi.org/10.1175/JPO-D-14-0167.1

Whalen, C. B., Talley, L. D., & MacKinnon, J. A. (2012). Spatial and temporal variability of global ocean mixing inferred from Argo profiles. *Geophysical Research Letters*, *39*, L18612. https://doi.org/10.1029/2012GL053196

Wijesekera, H., Padman, L., Dillon, T., Levine, M., Paulson, C., & Pinkel, R. (1993). The application of internal-wave dissipation models to a region of strong mixing. *Journal of Physical Oceanography*, *23*(2), 269–286. https://doi.org/10.1175/1520-0485(1993)023<0269:TAOIWD>2.0.CO;2

Wunsch, C., & Ferrari, R. (2004). Vertical mixing, energy, and the general circulation of the oceans. *Annual Review of Fluid Mechanics*, *36*, 281–314. https://doi.org/10.1146/annurev.fluid.36.050802.122121

Yilmaz, Ö. (2001). *Seismic data analysis: Processing, inversion, and interpretation of seismic data* (2065 pp.). Tulsa, OK: Society of Exploration Geophysicists. https://doi.org/10.1190/1.9781560801580

Zenk, W., & Katz, E. J. (1975). On the stationarity of temperature spectra at high horizontal wave numbers. *Journal of Geophysical Research*, *80*(27), 3885–3891. https://doi.org/10.1029/JC080i027p03885